Adv Polym Sci (2011) 241: 187–249
DOI:10.1007/12_2010_56

Fluorescence Spectroscopy as a Tool for Investigating the Self-Organized Polyelectrolyte Systems

Karel Procházka, Zuzana Limpouchová, Filip Uhlík, Peter Košovan, Pavel Matějíček, Miroslav Štěpánek, Mariusz Uchman, Jitka Kuldová, Radek Šachl, Jana Humpolíčková, and Martin Hof

Abstract In this article, we outline the principles and application of several time-resolved fluorescence techniques for studying the behavior of stimuli-responsive self-assembled polymer systems. We demonstrate the high research potential of fluorescence using results of several published studies performed by the research team at the Charles University in Prague in the framework of the Marie Curie Research Training Network “Self-Organized Nanostructures of Amphiphilic Copolymers” (MRTN-CT-2003-505027). We have chosen several interesting examples of complex self-assembling systems, the behavior of which could not have been understood without the help of targeted fluorescence studies. We have chosen four different techniques, two of them relatively popular (fluorescence anisotropy and nonradiative excitation energy transfer) and two only little used in polymer science (the solvent relaxation method and fluorescence correlation spectroscopy). The last part of the article is devoted to computer simulations (Monte Carlo and molecular dynamics) aimed at the interpretation of fluorescence data.

Keywords Block copolymer micelles · Fluorescence anisotropy · Fluorescence correlation spectroscopy · Molecular dynamics simulations · Monte Carlo simulations · Solvent relaxation method · Time-resolved fluorescence

---

K. Procházka (✉), Z. Limpouchová, F. Uhlík, P. Košovan, P. Matějíček, M. Štěpánek, M. Uchman, and J. Kuldová
Department of Physical and Macromolecular Chemistry, Faculty of Science, Charles University in Prague, Albertov 6, 12843 Prague 2, Czech Republic
e-mail: prochaz@vivien.natur.cuni.cz; zl@vivien.natur.cuni.cz; uhlik@sals.natur.cuni.cz; kosovan@vivien.natur.cuni.cz; matej@vivien.natur.cuni.cz; stepanek@natur.cuni.cz; mariuszuchman@o2.pl; jh@vivien.natur.cuni.cz

R. Šachl, J. Humpolíčková, and M. Hof
The Jaroslav Heyrovsky Institute of Physical Chemistry, Czech Academy of Sciences, Dolejškova 5, Prague 8, Czech Republic
e-mail: radek.sachl@jh-inst.cas.cz; jana.humpolickova@jh-inst.cas.cz; martin.hof@jh-inst.cas.cz

Contents

Abbreviations

An	Anthracene
c.m.c.	Critical micelle concentration
DLS	Dynamic light scattering
FCS	Fluorescence correlation spectroscopy
fwhm	Full width in half-maximum
IC	Internal conversion
ISC	Intersystem crossing, intersystem conversion
LCST	Lower critical solution temperature
LS	Light scattering
MC	Monte Carlo
MD	Molecular dynamics
M_n	Number-average molar mass
M_w	Weight-average molar mass
NMR	Nuclear magnetic resonance spectroscopy
Np	Naphthalene
NRET	Nonradiative excitation energy transfer
ORB	Octadecyl rhodamine B
PAA	Poly(acrylic acid)

PE	Polyelectrolyte
PEO	Poly(ethylene oxide)
PMA	Poly(methacrylic acid)
PS	Polystyrene
PVP	Poly(2-vinylpyridine)
rhs	Right hand side
SLS	Static light scattering
SRM	Solvent relaxation method
TCSPC	Time-correlated single photon counting
TRES	Time-resolved emission spectra
TRFS	Time-resolved fluorescence spectroscopy

1 Introduction

For several decades, fluorescence spectroscopy has been one of the most frequently used techniques for studying the conformations and dynamics of synthetic and natural macromolecules. The versatility and broad applicability of fluorescence techniques for investigation of both static and dynamic properties of different systems stems from two grounds:

1. Fluorescence, i.e., the emission of a photon due to a spontaneous spin-allowed transition from the excited to the ground state, is a phenomenon concerning an energetically rich species (excited fluorophore) that strongly interacts with surrounding molecules. Hence, this phenomenon is influenced by interactions of the fluorophore with its microenvironment and yields indirect information on properties of the host system in which the fluorophore is embedded. Because the fluorophore "feels" the effect only of neighboring molecules, fluorescence techniques can be used for probing very small spatial regions. This offers the possibility to investigate small domains in nano-to-meso-heterogeneous systems, where most of common macroscopic techniques fail. Some fluorescence characteristics (e.g., the excitation and emission wavelength) depend both on interactions of the fluorophore in the ground and excited state, and others (e.g., the fluorescence lifetime) on interactions in the excited state only. This generates certain diversity in the dependence of individual fluorescence characteristics on the properties of the host system and broadens the research potential.
2. The second fact that enables monitoring fast dynamic processes is that the excitation (absorption of a photon) and the "red-shifted" fluorescence emission are two events separated by a time-window ranging from units to hundreds of nanoseconds (depending on the fluorophore and the surrounding medium). On this timescale, a number of molecular processes proceed, e.g., translational and rotational diffusion of the fluorophore in a small volume comparable with the range of interactions, reorientation of molecules in the solvate shell, segmental dynamics of

> flexible polymer chains, and nonradiative energy transfer due to dipole–dipole interactions. All those processes affect the fluorescence characteristics. The advanced fluorescence measurements introduced about 40 years ago with a time resolution corresponding to the rate of these processes (i.e., nanosecond and subnanosecond time-resolved fluorescence measurements) almost immediately opened a new field of study of fast processes at the molecular level.

As a result of enormous development in the technology and production of pulse lasers, laser diodes, detector systems, and powerful computers in recent decades, steady-state and time-resolved fluorometers now belong to the standard equipment of biochemical and macromolecular laboratories. For example, there are apparatuses combined with microscopes that are suitable for time-resolved fluorescence measurements of individual organelles in living cells. However, the widespread use of fluorescence techniques generates certain danger, which is connected with their routine use. We would like to point out that the fluorescence spectroscopy is an indirect technique and that the interpretation of results needs great care and precaution. It almost always requires additional information on the system.

When designing a fluorescence experiment and interpreting data, one more possible complication has to be kept in mind: Only a limited number of systems involve intrinsic fluorophores and are inherently luminescent. Such systems (e.g., proteins containing tryptophan) are very suitable for fluorescence studies and reliable information on the location, mobility, and accessibility of tryptophane residues can be obtained in a relatively straightforward way. In other cases, an extrinsic fluorescence probe has to be added to the system. Its addition modifies the system, which can be a problem (more or less severe) depending on the system studied and on the fluorescence technique used. Because the fluorescence reports on the behavior of the microenvironment of the probe, it does not yield information on the original system, but only on its small perturbed part, even though the overwhelming part of the system has not been altered at all and behaves as the system without added fluorophore. It is obvious that an attempt to reduce the probe content in the host system could partially suppress this problem, but would not eliminate it entirely.

The aim of this feature article is to outline our application of fluorescence techniques to polymer self-assembly studies. We do not intend to give a complete survey of the use of fluorescence in polymer chemistry. We focus only on techniques that we have been using within the POLYAMPHI network. We start with a description of the principles of fluorescence phenomena and an explanation of the role of processes that influence the rates of transition and the spectroscopic characteristics. Then we discuss several examples of our experimental studies, in which we applied different variants of time-resolved measurements. Finally, we show how computer modeling can be used to support the interpretation of data on complex systems.

2 Principles of the Fluorescence Techniques Used

2.1 *State Diagram and the Characteristics of Time-Dependent Fluorescence*

The most comprehensive description and explanation of all processes that affect the fluorescence and the role of additional external factors is provided by the Jablonski diagram (Fig. 1), which represents the scheme of energy levels of electronic and vibrational states of a molecule and the possible transitions [1].

The vertical axis indicates increasing energy of different quantum states in vacuo or the Gibbs free energy of the fluorophore in condensed systems (e.g., in solutions). Individual states corresponding to the optimum molecular geometry are depicted by horizontal lines. The arrows indicate possible transitions between different states. Typical values of rate constants of all processes have been also included.

Prior to excitation, the molecule is in the lowest vibrational state of the lowest electronic state (ground state), S_0. The absorption of a photon is governed by optical selection rules [2]. Its probability is proportional to the square of the transition dipole moment. The most severe restriction concerns the spin conservation. Further restrictions reflect the symmetry and overlap of corresponding wave functions. Regardless of the probability (reflected by the molar absorption coefficient), the single act of transition to a higher excited state due to absorption of a photon belongs to the fastest processes that occur in nature (except nuclear processes) and proceeds on timescales shorter than 10^{-15} s [3]. In this short time, neither the position of

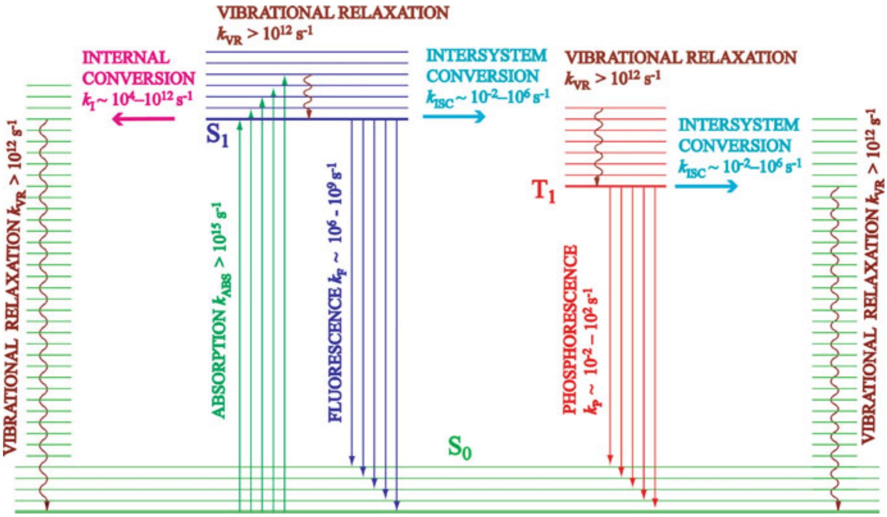

Fig. 1 The Jablonski diagram: the energies of the ground electronic singlet state S_0, excited singlet S_1, and triplet T_1 are depicted by *bold horizontal lines*; vibrational states by *narrow lines*; the most important transitions are depicted by *arrows* and *wavy lines*; the typical values (in orders of magnitudes) of rate constants of the processes have been also included

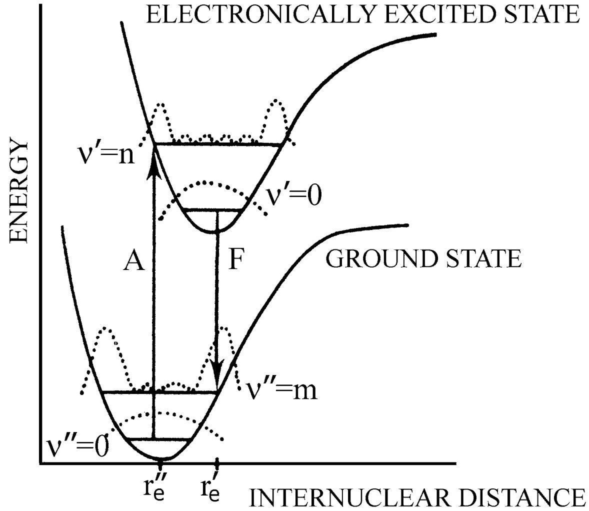

Fig. 2 The Franck–Condon principle: the energies of the ground and the first excited singlet states, S_0 (*lower curve*) and S_1 (*upper curve*), respectively, of a diatomic molecule are presented as functions of the distance between atoms, r. The probabilities of distances, r, are depicted by *dotted curves*; the *vertical arrows A* and *F* stand for absorption and emission, respectively

nuclei nor of surrounding molecules change and the excitation proceeds adiabatically without interaction with the environment. Immediately upon excitation, the molecule still keeps its ground state geometry (the Franck–Condon principle) [4, 5]. The excitation of a diatomic molecule is depicted in more detail in Fig. 2. Here, the energies of the ground and excited states (together with several vibrational levels) are drawn as functions of the distance between the atoms. The scheme is supplemented by several vibration wave functions to see the spatial overlap. The spatial overlap of wave functions shows that the absorption generates both the electronic and vibration excited state.

The vibration relaxation proceeds in most nonviscous solutions at timescales of 10^{-14}–10^{-12} s [6]. The excess energy is transferred to the surrounding medium during collisions of vibrating molecules with solvent molecules efficiently and quickly, because the collisions proceed roughly at the same frequency as vibrations (i.e., 10^{12}–10^{14} collisions s^{-1}) and the masses of colliding species are comparable. The series of nonradiative relaxation processes in the excited state involves one more process – the relaxation of the microenvironment that proceeds only in condensed polar systems. This process will be discussed in detail below (see Sect. 2.3).

So far, we have considered only the excitation to S_1. If the molecule is excited to a higher electronic state (S_2, S_3, etc.), in the overwhelming majority of cases, it reaches the lowest excited singlet state S_1 on the picosecond timescale by a cascade of nonradiative (vibration relaxation) processes and only then can the emission of a photon occur. There exist only a few exceptions from this rule, e.g., azulene [7], which exhibits fluorescence from S_2.

When describing the fluorescence as an observable spectroscopic phenomenon, we have to discuss the depletion of the excited state in a large ensemble of molecules. Even though the concentration of fluorophores and the fraction of excited molecules in fluorescence measurements are low (typically 10^{-6}–10^{-5} mol L^{-1} and less than 10^{-6}, respectively), the common steady-state irradiation generates about 10^9 excited molecules per milliliter. The depletion of the excited state is a stochastic process that involves a number of independent competing contributions, both radiative (fluorescence) and nonradiative (internal conversion or intersystem crossing to the triplet state T_1, both followed by the vibration relaxation). The probabilities (and rate constants) of individual contributing processes depend on the chemical nature of the molecule (on its spectroscopic properties) and on interactions with surrounding molecules.

The process that we are interested in, is the spin-allowed $S_1 \rightarrow S_0$ emission of a photon (fluorescence). Analogously to the absorption, its probability depends on the change of the dipole moment during the transition. It also depends on the energy difference between S_0 and S_1 [3]. For a fully allowed (spin, symmetry, overlap allowed) spontaneous emission, the quantum mechanics calculations predict a rate constant of about 10^9 s^{-1}. This means that the natural lifetime of the excited state of most molecules are in nanoseconds and that the depletion rate, measured as the number of excited photons per time unit (light intensity), after a short excitation pulse decays (in a simple case exponentially) on the nanosecond timescale. The observed lifetimes are often much shorter because different nonradiative processes contribute significantly to the depletion of the excited state. In some cases, they can be longer (10^1–10^2 ns) if the transition is not fully allowed, e.g., (a) the symmetry rule is not obeyed, but antisymmetric vibrations relax the selection rules or (b) the spatial overlap of the ground and excited state wave functions is small.

Because the probabilities of absorption and emission depend on dipole moments in the same states, there exists a straightforward (linear) relationship between the molar absorption coefficient and the rate constant of the spontaneous emission (the higher the probability of absorption, the higher the emission) [7]. However, the observed fluorescence intensity is often much weaker than that expected, because the competitive nonradiative processes can deplete the excited state much faster than fluorescence. Hence, according to the Franck–Condon principle, the molecule finishes in a higher vibrational level of the ground state S_0. Then, a fast vibrational relaxation takes place that causes the intrinsic Stokes shift (the red shift of fluorescence with respect to absorption) [8]. One more fact is important and should be kept in mind for further discussion: the absorption and emission of a photon by a particular molecule are two almost infinitely fast events, but they are separated by a time window of nanoseconds.

There exist a number of competing nonradiative processes that deplete the excited state and quench the fluorescence. The first one is the internal conversion, IC. Its rate varies over a wide range of orders of magnitudes. Its probability (efficiency) depends on the structure and properties of the molecule and on interaction with surrounding molecules. It can be affected experimentally, e.g., by the choice of solvent. For flexible and strongly interacting molecules, the process can proceed on the picosecond timescale and can deplete the excited state before the considerably slower emission occurs. This explains why most molecules do not exhibit any fluorescence at all and only fairly rigid molecules are strongly emitting fluorophores, and why the fluorescence intensity increases in viscous solvents, at low temperatures (when the mobility of molecules and both the frequency and energy of collisions decreases), and in nonpolar solvents (where the interactions with solvent molecules are relatively weak).

Another important nonradiative process is the $S_1 \rightarrow T_1$ intersystem crossing, ISC. This transition is strictly forbidden by the spin-selection rule [2], but the selection rule is in reality relaxed by spin–orbital interaction in many systems that contain heavy atoms in the molecule (in this respect, the adjective "heavy" is relative: even carbon is heavy enough to break the rule). The probability (rate) of ICS depends on the energy difference between S_1 and T_1. For molecules with energetically close S_1 and T_1 states, the process can be very efficient (k_{ISC} ca. 10^{12} s^{-1}) due to the resonance effect and intermixing of S_1 and T_1 states. For other molecules with a large energy difference between the excited singlet and triplet state, the role of ISC is negligible.

After the $S_1 \rightarrow T_1$ transition, the molecule finishes in a dangerous situation. It contains a lot of excess energy and is therefore more reactive than in the ground state. The probability of photon emission and its return to the ground state S_0 (phosphorescence) is low because it represents the spin-forbidden transition and, in this case, the difference between T_1 and S_0 energies is large. The danger derives from a high probability of collisions with other molecules, which can cause a photochemical reaction and creation of a new chemical species (i.e., destruction of the original one). Indeed, most photochemical reactions involve molecules in T_1 state (as reactants, photosensitizers, etc.) [3]. It follows from the above outline that the phosphorescence is red-shifted with respect to fluorescence and that its intensity is usually very low due, in part, to its low natural rate (rate constants k_{P} ca. 10^{-3}–10^{3} s^{-1}) and to efficient competitive nonradiative depletion of the T_1 state (mostly by vibrational relaxation, collision energy transfer, etc.). In some cases (if S_1 and T_1 states are energetically close), the molecule can gain enough energy either during collision with non-reactive solvent molecules or as a result of triplet–triplet annihilation and return to S_1. In this case, delayed fluorescence can be observed [3], but we will not discuss this process in detail.

Before we finish the general outline, a few characteristics have to be defined. The total rate constant of the depletion of the excited state S_1 is the sum of rate constants of all monomolecular depletion processes, $k_{\mathrm{tot}} = \sum k_i$. If some bimolecular processes such as collision quenching contribute, then the corresponding terms would be the products of the pertinent bimolecular rate constants and quencher concentrations. The fluorescence quantum yield is the ratio of photons emitted per given number of absorbed photons, $q_{\mathrm{F}} = N_{\mathrm{em}}/N_{\mathrm{abs}}$. It is (in contrast to the quantum yield of chemical reactions) always lower than 1 and it can be expressed as the ratio of time constant of fluorescence and the total rate constant, $q_{\mathrm{F}} = k_{\mathrm{F}}/k_{\mathrm{tot}}$. Analogously the quantum yields of other processes can be defined.

In an ensemble of equivalent fluorophores (which concerns both their chemical structure and environment), e.g., in a dilute solution, the fluorescence intensity after excitation with an ultrashort pulse decays exponentially. The experimental fluorescence lifetime (time in which fluorescence decays to 1/e of the initial value), τ_F, is the reciprocal value of k_{tot} ($\tau_F = 1/k_{tot}$). If individual fluorophores experience different microenvironments (in heterogeneous systems), their emission wavelengths and decay times differ and therefore the emission band is fairly broad, sometimes bimodal or multimodal and the decay is no longer single-exponential.

In the time window between the absorption and emission of a photon, a number of molecular processes can occur. They concern either (a) the fluorophore itself (its rotational and translational diffusion, conformational changes, transition between electronic states differing in dipole moment) or (b) molecules in its immediate vicinity (reorganization of the solvent shell, diffusion of quenchers, etc.). All these processes influence the fluorescence properties (position and shape of the emission band, quantum yield, decay time, etc.). In most cases, both the fluorophore and the surrounding molecules participate in the process and fluorescence characteristics are in fact influenced by their mutual interactions. Figure 3 shows a survey of important

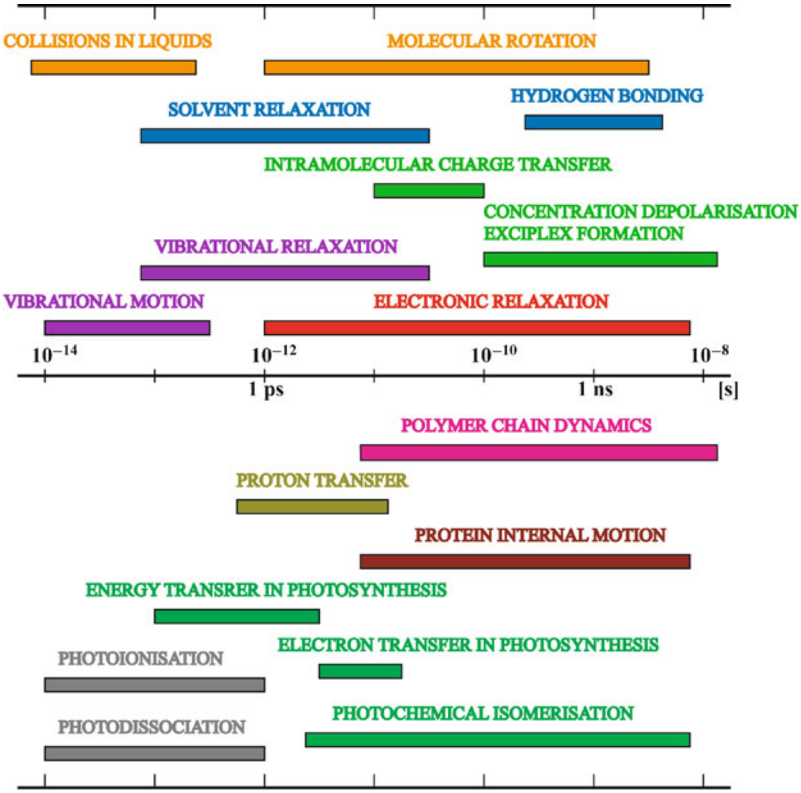

Fig. 3 The outline of fast dynamic processes: the rate of the polymer chain dynamics (vibrational motion and relaxation) strongly overlaps that of electronic relaxation and can be studied by the time-resolved fluorescence

dynamic processes that proceed at comparable velocities with the depletion of the S_1 state and can be studied by time-resolved fluorescence spectroscopy (TRFS). Some of them will be addressed in more detail in Sect. 2.2.

2.2 Time-Resolved Fluorescence Anisotropy

The photon absorption probability by a given molecule depends on a magnitude of the absorption dipole moment, $\boldsymbol{\mu}_{\mathrm{A}}$, and on its orientation with respect to the excitation polarization described by the angle ϕ. The molecules with their transition dipole moment parallel to the excitation polarization are excited preferentially, while those oriented perpendicular are not excited at all. For a general orientation, the dipole moment can be decomposed into parallel and perpendicular components, $\boldsymbol{\mu}_{\mathrm{A}}$ $\cos\phi$ and $\boldsymbol{\mu}_{\mathrm{A}}$ $\sin\phi$, respectively, and the excitation probability is simply proportional to ($\cos\phi$). The absorption and emission transition dipole moments, $\boldsymbol{\mu}_{\mathrm{A}}$ and $\boldsymbol{\mu}_{\mathrm{E}}$, can form any angle, ω; however, they are usually parallel in fluorophores containing symmetry planes.

Although the fluorophores are usually oriented randomly before the excitation (e.g., in solutions), the population of excited molecules with $\boldsymbol{\mu}_{\mathrm{A}}$ parallel with respect to excitation polarization dominates immediately after the short polarized excitation pulse. The anisotropic orientation of excited molecules starts to relax due to the rotational Brownian motion of fluorophores and the excitation energy migration among fluorophores. The rate of the latter process depends strongly on the distance between fluorophores, and an appropriate dilution suppresses its effect considerably. The relaxation can be monitored by measuring the time-resolved fluorescence anisotropy, which is defined as $r(t) = [I_{\mathrm{II}}(t) - I_{\perp}(t)] / [I_{\mathrm{II}}(t) + 2I_{\perp}(t)]$, where $I_{\mathrm{II}}(t)$ is the parallely polarized and $I_{\perp}(t)$ is the perpendicularly polarized fluorescence intensity with respect to the excitation pulse.

The theory shows that the time-resolved fluorescence anisotropy $r(t)$ is the autocorrelation function of orientations of the absorption dipole moment at the instant of excitation of a molecule, $\boldsymbol{\mu}_{\mathrm{A}}(t=0)$, and that of emission at the time t, $\boldsymbol{\mu}_{\mathrm{E}}(t) : r(t) = 2/5\ \langle P_2\,(\boldsymbol{\mu}_{\mathrm{A}}\,(t=0)\,\boldsymbol{\mu}_{\mathrm{E}}\,(t))\rangle$, where P_2 stands for the Legendre polynomial of the second order and brackets $\langle\rangle$ denote the ensemble averaging. The initial anisotropy, $r(t=0) = r_0 = 0.6\cos\omega - 0.2$ depends on the angle ω between $\boldsymbol{\mu}_{\mathrm{A}}$ and $\boldsymbol{\mu}_{\mathrm{E}}$ and varies between limiting values -0.2 and 0.4, for perpendicular and parallel orientation of $\boldsymbol{\mu}_{\mathrm{A}}$ and $\boldsymbol{\mu}_{\mathrm{E}}$, respectively.

In many fluid systems, the rotational diffusion proceeds at the timescales comparable with the fluorescence decay and can be used for studying the viscosity of the microenvironment, local geometrical constraints, segmental motion of polymer chains, etc. In non-viscous solvents, it decays usually faster than fluorescence, but in very viscous systems a full randomization occurs at times much longer than the fluorescence lifetime. The extrapolation to $t \to \infty$ yields the residual anisotropy, r_∞. In the case of some polymer systems with entrapped fluorophores, only a partial (i.e., locally anisotropic) orientation reorganization of the fluorophore proceeds and therefore r_∞ can give a non-zero value.

There exist a number of models predicting the time evolution of $r(t)$ for small fluorophores in the solution. They differ in accuracy and detail of physical description and in mathematical approximations. The simplest rotational model is based on the Debye hydrodynamic theory [9]. It assumes that the rotational diffusion proceeds in small steps between collisions of the fluorophore with surrounding molecules. An analytical expression for $r(t)$ as a sum of several exponentials was first derived by Favro [10]:

$$r(t) = \sum_i A_i \exp\left(-\frac{t}{\tau_{c,i}}\right). \tag{1}$$

The number of terms (up to five, but only three of them independent) and values of pre-exponential factor A_i depend on the fluorophore symmetry and on the orientations of $\boldsymbol{\mu}_\mathrm{A}$ and $\boldsymbol{\mu}_\mathrm{E}$ in the molecule. The rotation correlation times, $\tau_{c,i}$, reflect the main components of the gyration tensor only. For the parallel orientation of both dipole moments, the initial anisotropy in a fluid system has the highest possible value, $r_0 = \sum_i A_i = 0.4$. In the case of a spherical rotor, fluorescence anisotropy reduces to a single exponential function. For a symmetric rotor, $r(t)$ is either single- or double-exponential, depending on the orientation of dipole moments with respect to the long axis.

A typical time evolution of fluorescence anisotropy is a monotonously decreasing function. However, the sum of several exponentials with both positive and negative prefactors derived on the basis of a rigid rotor model does not preclude increasing or even a non-monotonous time evolution. The non-monotonous time evolution has been observed for perylene excited to S_2 quite far in the "blue region" with respect to the emission [11]. It starts, as predicted for the perpendicular orientation of dipole moments, at $r_0 = -0.2$, but increases rapidly to a slightly positive transient value and then decreases more slowly to $r_\infty = 0$. The non-monotonous $r(t)$ decay can be rationalized by the solvent effect on the rotation of the flat disc-like perylene around three different axes.

If the fluorophore contains several energetically close excited states differing in the polarization direction [12, 13], the excitation to higher states is usually followed by a few vibrational relaxations routs. In this case, the emission is strongly depolarized from the very beginning and the anisotropy measurement is useless. However, a similar depolarization occurs if the angle ω (quite common for low-symmetry fluorophores) is close to the magic angle, $\gamma = 54.7^\circ$. In this case, $\cos\gamma = 1/3$ and the fluorescence is depolarized at $t = 0$.

The rigid rotor model has been currently used for small fluorophores, but it is not suitable for tagged or labeled polymers. In this case, $r(t)$ monitors a combination of a fast rotation of the fluorophore around one or several single bonds attaching it to the polymer backbone, and a slower complex motion of a part of the chain together with the fluorophore. The relatively slow rotation of the whole polymer coil proceeds on a longer timescale than the fluorescence decay and is "invisible" in the time-resolved fluorescence measurement. It can be detected as a significant residual anisotropy. Therefore, the anisotropy decay is often fitted to a double-exponential function with a constant term r_∞. There exist several models describing the behavior of labeled polymers with fluorophores embedded in the main chain. A convenient formula has been derived by Valeur and Monnerie [14] in the form: $r(t) = r_0 \exp(-t/\tau)\exp(-t/\rho)\,\mathrm{erfc}\sqrt{t/\rho}$, where r_0 is the initial anisotropy, and τ and ρ are two rotation correlation times describing a perturbed "crankshaft motion" of several successive polymer segments. This model reflects the facts that (a) fast local motion of segments resembles the rotation of a crankshaft, and (b) simultaneous distortion of several successive dihedral angles lowers the corresponding rotational barrier considerably.

For successful monitoring of the microviscosity, one aspect is very important: the emission wavelength of the probe should not be polarity-dependent. In many systems, the solvent relaxation proceeds at a comparable timescale with the rotational diffusion of the probe (see Sect. 2.3), the shape of fluorophore with its solvate shell continuously changes, and the emission maximum shifts with time. In such a case, the anisotropy measurements at different wavelengths yield different rotation correlation times, because the red-shifted decay reflects the behavior of a more relaxed state than that measured in the blue part of the emission band [15].

Some information on the microviscosity can also be obtained by steady-state anisotropy measurements. A comparison of results for different media (e.g., for a series of mixed solvents differing in composition) is tricky and requires the measurement of fluorescence lifetimes. The steady-state anisotropy, $\langle r \rangle$, is a time-average weighted by the fluorescence intensity decay, $I(t)$:

$$\langle r \rangle = \frac{\int_0^\infty r(t)I(t)\mathrm{d}t}{\int_0^\infty I(t)\mathrm{d}t}. \tag{2}$$

From (2), it is evident that the average value depends on the fluorescence lifetime and that the long-living probes always yield low $\langle r \rangle$. The best probe for anisotropy measurement should have a little faster $r(t)$ than $I(t)$ decay. The same condition applies for the time-resolved studies. If $I(t)$ decays much faster than $r(t)$, only a small portion of $r(t)$ is accessible. In the opposite case, the decay curves have to be measured with high statistics in a broad time range, but only small initial parts of $I_{\mathrm{II}}(t)$ and $I_\perp(t)$ curves are exploited for the evaluation of $r(t)$ decays. This prolongs needlessly the time-correlated single photon counting (TCSPC) time.

Fluorescence anisotropy studies are popular in biological and biochemical research of lipid membranes [16–18], proteins [19–22], etc. and also in polymer science. They have been performed for monitoring the conformations and flexibility of polymer chains in dilute, semidilute and concentrated solutions [23–27], in polymer melts and blends [28–31], and also for studying polymer self-assembly [32–34]. Nowadays, steady-state and time-resolved fluorescence anisotropy are currently used methods in polymer chemistry.

2.3 Solvent Relaxation

2.3.1 Theoretical Background

The solvent relaxation method (SRM) is a technique that provides unique information on the polarity and viscosity (more precisely on mobility) of the fluorophore solvate shell. Suitable probes should exhibit a large shift of their emission maxima to longer wavelengths in media with increasing polarity, but their photophysics should not be too complicated; that is, neither the position nor the shape of the emission band should be significantly affected by specific effects like hydrogen bonding, promoted dissociation in the excited state, charge transfer, structural changes, etc. Measurements with specifically interacting probes are possible and they have been applied in a number of studies, because such probes exhibit large changes in dipole moment upon excitation and sometimes offer additional advantageous properties. However, the interpretation of their behavior is not universal and needs very detailed knowledge of the probe photophysics [35]. Hence, we will confine the discussion to relatively simple probes and describe the technique that was originally developed and first applied for monitoring the relaxation behavior of the solvate shell in simple liquids. Popular probes for this purpose are coumarin dyes [36–38] or prodan [39–41], which undergo large dipole moment changes upon excitation and show quite regular polarity shifts. Now, we will explain the solvent relaxation for the case of a regular fluorophore dissolved in a simple liquid.

As already mentioned, the necessary condition for any radiative electronic transition (both for absorption and emission) is the change of the dipole moment of the molecule. The solvent relaxation process is depicted in Fig. 4 for a fluorophore that is immersed in a polar solvent and has the excited state dipole moment, $\boldsymbol{\mu}^*$, higher than that in the ground state, $\boldsymbol{\mu}$. The vertical axis shows the Gibbs free energy of the solvated fluorophore. Prior to excitation, the optimum arrangement and orientation of polar solvent molecules in the solvation shell of the fluorophore (with respect to its dipole) minimizes the Gibbs free energy of the system. Solvent molecules are usually small as compared with the fluorophore and they catch up both with its translational and rotational diffusion.

The absorption of a photon occurs in less than 10^{-15} s and the "electron cloud" redistribution and the consequent change of the dipole moment, $\Delta\boldsymbol{\mu} = \boldsymbol{\mu}^* - \boldsymbol{\mu}$, of the fluorophore (precisely of its electronic part) are almost immediate processes as compared with the rates of motions of nuclei within the fluorophore and surrounding molecules. This means that immediately upon excitation, the geometry of the fluorophore and the arrangement of molecules in the solvate shell correspond to the ground state. The solvation is not the optimum one and the Gibbs free energy of the solvated fluorophore at early times after excitation is higher than that in the equilibrium state.

The orientation polarization motions of solvent molecules necessary for optimum reorganization of the solvent shell are slower than the vibrational relaxation of the fluorophore, and the free energy after the vibrational relaxation is therefore higher than that in the equilibrium state. Although the vibrational relaxation is a process

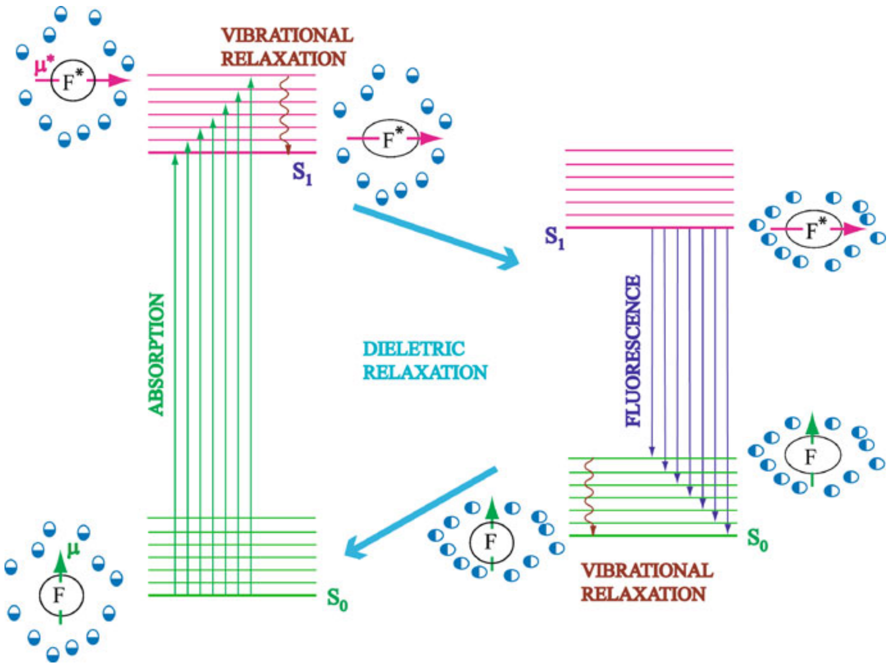

Fig. 4 Solvent relaxation: energies of the electronic states of a solvated fluorophore are depicted by *bold lines*, vibrational states by *thin lines*; the long arrows and *wavy lines* show individual processes; the changes of the dipole moment and geometry of the fluorophore upon excitation and emission are depicted by different orientations of the *short arrow* and the ellipsoidal prolongation. The changes in the arrangement and orientation of polar solvent molecules are also indicated

that occurs independently of the solvent polarity, the solvent relaxation proceeds only in polar solvents. Its extent is given by the strength of the dipole–dipole interaction between the fluorophore and the molecules in the solvate shell (local polarity of the nanoenvironment), while its rate reflects the mobility of the solvate shell (local viscosity of the nanoenvironment). In non-viscous solvents, the solvent relaxation can be quite fast and may partially overlap with the vibrational relaxation.

The next process is the emission of a photon. As already mentioned, the emission of photons in a macroscopic system of fluorophores proceeds on the nanosecond timescale. This means that most photons are usually emitted and detected from excited states with fully relaxed solvate shell. Because the excited state population decays exponentially, fast measurements enable detection of “hot” photons from non-relaxed states at early times. When discussing the relaxation at the level of a single molecule, we have to consider different timescales. An isolated single emission event is as fast as the absorption, and the electronic transition takes less than 10^{-15} s. It is evident that the fluorophore does not reach the relaxed ground state immediately after the emission of a photon. What follows, is a cascade of processes that resemble the mirror image of the above-described relaxations. Firstly, the vibrational relaxation occurs and, finally, the solvent equilibrates corresponding to the ground state dipole. The above description explains the red-shift of the emission of common fluorophores in polar solvent, which is an experimentally recognized phenomenon known as the Stokes shift.

The simplest quantitative treatment of the solvent relaxation assumes that the fluorophore is placed in the cavity of radius a in the medium characterized by the relative dielectric permittivity ε and the refractive index n. It yields the Lippert equation [42] for the wavenumber shift between absorption and emission maxima of the fully relaxed host system:

$$\Delta\nu = \frac{2\,(\mu^{*}-\mu)^{2}}{hca^{3}}\left(\frac{\varepsilon-1}{2\varepsilon+1}-\frac{n^{2}-1}{2n^{2}+1}\right), \tag{3}$$

where h is the Planck constant and c is the light speed in vacuum. This equation offers the possibility to probe local polarity in heterogeneous systems (providing that the partitioning of the fluorophore between different domains is known).

2.3.2 Specific Features of Solvent Relaxation in Heterogeneous Systems

The majority of experimental works have addressed solvent relaxation in biological systems such as lipid membranes [43–45], proteins [46, 47], or nucleic acids [48], although a number of low-molar-mass systems have also been investigated [49–51]. Recently, very interesting relaxation processes on a relatively slow (nanosecond) timescale have been discovered in low-molar-mass solvent mixtures, reflecting the redistribution of solvent components in the solvate shell [52–54]. A couple of research groups have turned their attention to surfactants and polymeric nanoparticles (Pluronics micelles, etc.) [55, 56]. In the following discussion, we will focus on systems containing water-soluble nanoparticles with preferentially adsorbed probes that we studied experimentally. We will outline the strategy and goals of our studies and describe the methodology that we developed.

The studied aqueous system contains (a) relatively large polymeric nanoparticles, either simple spherical core–shell micelles or multilayer (onion skin) micelles, the hydrodynamic radius of which ranges from a few tens to one hundred nanometers; (b) much smaller fluorescence probes (units of nanometers), which have high affinity to the nanoparticle (otherwise they would escape in bulk solvent and would not report on the nanoparticle); and (c) even smaller solvent molecules. The fluorescent molecules are either hydrophobic or amphiphilic (fluorescent surfactants with a long hydrophobic tail and a water-soluble, often electrically charged fluorescent head group) and they bind in specific nanodomains in the core or close to the core–shell interface. The system is dilute, but the probes are localized either inside the nanoparticle or in the vicinity of its surface, where the concentration of polymer units is high. The discussion will be confined to fluorescent surfactants that physically bind in the inner part of the water-soluble shell of micelles formed by hydrophobic–hydrophilic copolymers. In contrast to the low-molar-mass solutions studied by SRM, the system is locally concentrated and strongly anisotropic.

The properties of the shell [density of polymer units, ionization degree (in weak polyelectrolyte shells), ratio of free-to-bound (solvating) water molecules, effective dielectric permittivity, etc.] change in the radial direction from the core–shell interface. In dense parts of the shell, the fluorophore often competes for water molecules with water-soluble polymer units. The relaxation of the solvate shell is very complicated compared with isotropic systems of small molecules and contains several contributions that differ significantly in relaxation rates. The complexity (when understood) offers an opportunity for detailed analysis, but a reliable knowledge of the behavior obtained by an independent method is indispensable. The time-resolved Stokes shift provides indirect information both on the solvation (hydration) of water-soluble polymer chains and on the segmental dynamics, because water molecules are engaged in the solvation of polymer segments, their motion is slowed down and coupled with segmental dynamics of polymer chains. If the affinity of the fluorophore to the nanoparticle is not high enough, the fluorescent part can move after excitation in the radial direction with respect to the nanoparticle and can experience higher microenvironment polarity during the lifetime of the excited state. This applies, e.g., to fluorescent surfactants with a short aliphatic tail that are not strongly anchored to the hydrophobic core. It is thus obvious that it is impossible to offer a universal scheme for the interpretation of solvent relaxation curves for systems containing fluorophores bound to nanoparticles. In Sect. 3.3, we will demonstrate that a careful analysis of data obtained by a combination of fluorescence SRM measurements with other experimental techniques provides details that are otherwise inaccessible, and that such an analysis helps to formulate reliable conclusions on the system behavior. As already mentioned, SRM has been very little used in polymer research so far. The main goal of pertinent parts of the paper is to “advertise” this technique and show its scientific potential.

2.4 Fluorescence Quenching and Nonradiative Excitation Energy Transfer

2.4.1 Fluorescence Quenching

In the preceding sections, it was shown that all nonradiative processes that compete with fluorescence shorten the fluorescence lifetime and weaken the emission intensity. Some of them, such as vibrational relaxation, depend on the fluorophore, solvent, and temperature. They predetermine the natural fluorescence lifetime, τ_{F0}, which is defined as the lifetime in the absence of any additional factors that can specifically quench the fluorescence. The molecules that strongly interact with the excited fluorophore are therefore called quenchers.

Fluorescence quenching requires a close approach of the quencher to the fluorophore and hence it can be used for studying various structural problems and dynamic processes. When both the fluorophore and quencher are dissolved in a solution, the time-resolved data report on the rate of diffusion. When the fluorophore is covalently attached to a polymer that segregates in aqueous media into hydrophobic and hydrophilic domains, study with a water-soluble quencher can answer the question of whether the labeled part of a polymer chain is accessible to water or not. Fluorescence quenching experiments are easy to perform and they have been used in biochemistry and in polymer science since the early 1950s [57].

One can distinguish two types of quenching processes: (a) dynamic (collision) and (b) static quenching. In the first case, the quencher (usually a transition or heavy metal ion, a complex containing a metal ion, a molecule containing a heavy atom, or oxygen) collides with excited fluorophore. During the contact, the excitation energy is transferred to the quencher and dissipates into the surrounding medium. This quenching affects the lifetime and consequently the emission intensity. Both fluorescence characteristics fulfill the well-known Stern–Volmer equation [58]:

$$\frac{F_0}{F} = \frac{\tau_{F,0}}{\tau_F} = 1 + K_{SV} c_Q, \tag{4}$$

where F_0 and F, and $\tau_{F,0}$ and τ_F are the steady-state fluorescence intensities and fluorescence lifetimes in the absence and presence of the quencher, respectively. K_{SV} is the dynamic Stern–Volmer constant, which is a product of the dynamic quenching rate constant k_q and the fluorescence lifetime in the absence of the quencher, $K_{SV} = k_q \tau_{F,0}$, and c_Q is the concentration of the quencher. If the motion of the fluorophore and quencher is a free diffusion, the dynamic quenching constant, k_q, is a product of the quenching efficiency, γ, and the diffusion-limited bimolecular rate constant for collision, k, which can be calculated from the Smoluchovski equation:

$$k = 4\pi D R_{mol} N_A, \tag{5}$$

where D and R_{mol} are the sum of diffusion coefficients and molecular radii, respectively, and N_A is the Avogadro number.

Quenching may also occur by a static process, which does not involve diffusion, due to a reversible formation of a nonfluorescent fluorophore–quencher complex in the ground state. In this case, part of fluorophore is incorporated into the complex and does not contribute to the fluorescence at all, and another part of the fluorophore exhibits the unaffected fluorescence with the natural fluorescence lifetime, $\tau_{F,0}$. The intensity of the fluorescence in the presence of the quencher is weaker, but the lifetime is unaffected. The Stern–Volmer plot is again linear and reads:

$$\frac{F_0}{F} = 1 + K_A c_Q, \tag{6}$$

where K_A is the association constant for the fluorophore–quencher complex. It is evident that a combination of steady-state and time-resolved measurements allows an unambiguous discrimination between pure static and dynamic quenching. An independent test can be based on measurements at different temperatures. Increasing temperature accelerates the rate of diffusion and generally promotes the dissociation of the complex. Hence, the slope increases with temperature for dynamic quenching and decreases for static quenching.

In many real systems, the Stern–Volmer plots are not linear due to various transient effects, which might lead to an up-curvature of the plot. On the other hand, an uneven accessibility of fluorophores in heterogeneous systems causes down-curvature and the leveling of the plot. Quite a number of models for analyzing fluorescence decays in specific systems have been proposed in the literature [8].

2.4.2 Nonradiative Excitation Energy Transfer

The nonradiative excitation energy transfer, NRET (called also the resonance or direct energy transfer), belongs to processes that quench the fluorescence of the excited fluorophore (donor) by transferring the excitation energy to another fluorophore (acceptor) over nanometer distances. Its mechanism was first elucidated by Förster about 60 years ago. In contrast to collision quenching, which requires a close approach of interacting species, Förster quenching assumes a "long range" electrostatic interaction of the dipole moment of the excited donor and acceptor in the ground state. The theory predicts that the interaction strength decays with r^{-6}, which limits the NRET effect for most practically important donor–acceptor couples to the nanometer range. The transfer concerns the short-living and only weakly interacting excited states of both fluorophores and proceeds under the condition of the conservation of total energy as a resonant process. The energy conservation requires that the excited electronic state of the acceptor is either the same or slightly less than that of the donor, because some excess energy can be dissipated in the vibrational energy. From the spectroscopic point of view, it means that the emission band of the donor has to overlap with the absorption band of the acceptor. If the interaction is purely dipolar and weak, and if the rate of transfer is proportional to the square of vibronic interaction energy, then the Förster formula holds for the transfer rate constant [59–61]:

$$k_{\mathrm{T}} = \left(\frac{1}{\tau_{\mathrm{d}}}\right)\left(\frac{R_0}{R}\right)^6, \tag{7}$$

where τ_{d} the fluorescence lifetime of the donor in the absence of the acceptor, R is the distance between donor and acceptor, and R_0 is the Förster radius, which is defined as the critical distance for which the rate of energy transfer is the same as that of fluorescence:

$$R_0 = \frac{9(\ln 10)\kappa^2 Q_{\mathrm{d}} J}{128\pi^5 n^4 N_{\mathrm{A}}}, \tag{8}$$

where κ^2 is the orientation factor for the dipole–dipole interaction (depending on the angle between the involved dipole moments), Q_{d} is the quantum yield of the donor emission in the absence of the acceptor, n is the refractive index, N_{A} the Avogadro number, and J is the normalized spectral overlap integral given by:

$$J = \frac{\int F_{\mathrm{d}}(\lambda)\varepsilon_{\mathrm{a}}(\lambda)\lambda^4 \mathrm{d}\lambda}{\int F_{\mathrm{d}}(\lambda)\mathrm{d}\lambda}, \tag{9}$$

where $F_\mathrm{d}(\lambda)$ is the emission spectrum of the donor (i.e., the fluorescence intensity of the donor in the absence of the acceptor at a given wavelength λ) and $\varepsilon_\mathrm{a}(\lambda)$ is the molar absorption coefficient at the wavelength λ. The energy transfer efficiency ξ_T is equal to $k_\mathrm{T}/(k_\mathrm{T} + k_\mathrm{F} + k')$, where k_T and k_F are the rate constant of the energy transfer and fluorescence decay, respectively, and k' is the sum of rate constants of all nonradiative de-excitation processes. ξ_T depends on the distance between the fluorophores, on the spectra overlap, and on the orientation factor κ^2 [62, 63]. This factor ranges from 0 to 4 depending on the orientation of fluorophores. It reaches the minimum value for the perpendicular orientation and the maximum value for the parallel and aligned orientation. Its evaluation causes some problems in experimental studies. For a random orientation of fast-rotating fluorophores, the averaging gives its "random dynamic" limit, $\kappa^2 = 2/3$.

Fluorescence quenching and NRET belong to popular fluorescence variants that have been exploited in a number of fields, including polymer and biopolymer research. NRET has been used in studies of polymer chain conformations [64–68], polymer miscibility [69–71], etc. Collision quenching, which reflects the accessibility of different quenchers, has been applied for testing the environment of pendant quenchers in polymer and biopolymer structures and associates [72–74]. Because the measurement is relatively simple, both techniques are "benchmark" fluorescence techniques in polymer science. Therefore, we could not avoid their use and, in spite of a number of review articles on that subject, we will briefly outline our results aimed at polymer self-assembly.

2.5 Fluorescence Correlation Spectroscopy

Fluorescence correlation spectroscopy (FCS) [75] is an optical method for studying dynamic processes, particularly the diffusion of intrinsically fluorescent or fluorescently labeled species, ranging from small molecules to nanoparticles. It has been widely used in biochemistry and biology [76–80], but its applications in polymer science [81, 82] are rather limited. In a typical experimental setup, the excitation beam passes through a very dilute (typically 10^{-9} M) solution of fluorescent particles and is focused in a very narrow region of roughly ellipsoidal shape. A small active (effective) volume, from which the signal (fluorescence emission) is detected, contains only a few fluorescent particles. The spatial profile of the excitation irradiation, $E(\boldsymbol{r})$, can be reasonably approximated by the Gaussian function:

$$E(\mathbf{r}) = E_0 \exp\left(-\frac{x^2+y^2}{2\omega_1^2} - \frac{z^2}{2\omega_2^2}\right), \tag{10}$$

where E_0 is the maximum intensity, $\boldsymbol{r} = (x, y, z)$ is the position with respect to the maximum irradiated center of the active volume and ω_1 and ω_2 are the half-axes of the ellipsoid and depend on the experimental setup. The fluorescent molecules undergo a translational diffusion motion, i.e., they enter and leave the active volume and visit places irradiated with different intensity of the excitation beam. This affects the probability of excitation and causes non-negligible fluctuations in the fluorescence intensity.

The time-resolved monitoring and evaluation of the autocorrelation function of the emission intensity fluctuations yield information on the diffusion rate of fluorescent species. However, the experimental measurement is affected by a number of parasite side effects. First, the intensity of the focused beam is very high, which promotes photobleaching (mainly the transition to the triplet state). Hence, only a few very stable and resistant fluorophores (rhodamine dyes or BODIPY) can be employed and still an appropriate correction has to be used when evaluating the diffusion coefficients. Second, the multiple labeling of particles of finite size can generate additional problems. We will focus on some of these complications in Sects. 3.5 and 4.3.

The quantity measured in FCS experiments is the autocorrelation function of the fluorescence intensity fluctuations, $G(\tau)$, defined as:

$$G(\tau) = \frac{\langle F(t)F(t+\tau)\rangle}{\langle F(t)\rangle^2}, \tag{11}$$

where $F(t)$ is the emission intensity at time t and τ is the lag time. When it is assumed that the motion of photophysically and photochemically stable point-like particles is strictly diffusive, and the excitation intensity profile is exactly Gaussian, an analytical expression for the autocorrelation function can be derived in the form [83]:

$$G(\tau) = 1 + \frac{1}{V_{\mathrm{eff}} c_{\mathrm{F}}} \left(1 + \frac{\tau}{\tau_{\mathrm{D}}}\right)^{-1} \left[1 + \left(\frac{\omega_1}{\omega_2}\right)^2 \frac{\tau}{\tau_{\mathrm{D}}}\right]^{-1/2}, \tag{12}$$

where τ_{D} is the characteristic diffusion time and c_{F} is the average concentration of fluorescent particles in the active (effective) volume, i.e., their macroscopic concentration if we neglect the potential "optical tweezer" effect of the strong electric field. The illuminated effective volume V_{eff} is defined as:

$$V_{\mathrm{eff}} = \frac{\left[\int_V E(\mathbf{r})\mathrm{d}^3\mathbf{r}\right]^2}{\int_V E^2(\mathbf{r})\mathrm{d}^3\mathbf{r}}. \tag{13}$$

The characteristic diffusion time, τ_{D}, is the typical time within which a particle diffuses over the diameter of the active volume. It is related to the translational diffusion coefficient $D = \omega_1^2/4\tau_{\mathrm{D}}$. Of the parameters of (12), only three are independent. The parameters of the optical setup, V_{eff} and ω_1/ω_2 ratio, can be determined beforehand from an independent measurement using a small fluorophore with known diffusion coefficient (e.g., rhodamine B). Thus, only two unknown parameters, c_{F} and τ_{D}, remain to be obtained from the experimental data fit.

When discussing the application of FCS in polymer science, it is instructive to compare its advantages and disadvantages with the dynamic light scattering

(DLS) method, which serves as a "benchmark" technique for measuring diffusion coefficients of polymers. For sufficiently large, strongly scattering polymers and polymeric nanoparticles, DLS is a generally applicable technique and yields more precise data because it is less affected by parasite side effects and requires the evaluation of a lower number of unknown parameters from the fit than does FCS. A further advantage of DLS in comparison with FCS consists in the exponential form of individual contributions to autocorrelation functions, which facilitates the treatment of polydisperse systems and/or separation of translational diffusion of the particles from their internal motions by means of inverse Laplace transformation. Last, but not least, the possibility of performing angular measurements provides an additional piece of information on the character of processes that generate fluctuations in the scattered light intensity.

In contrast to light scattering (LS) techniques, FCS can be used for a wider range of particle sizes, but it requires strong fluorescence of the studied species. This apparent drawback is often advantageous and FCS can be used for studying relatively small fluorescent particles in an excess of strongly scattering large particles. Careful design of the FCS experiment (proper choice of the extrinsic probe, exploitation of the dependence of the quantum yield on experimental conditions, etc.) can add other advantages. For example, fluorescent surfactants with a long aliphatic tail are hardly soluble in water and form self-quenched dimers and trimers at concentrations well below the critical micelle concentration (c.m.c.). They bind strongly to polymeric nanoparticles in the form of monomers and the emission increases after binding. Hence, the partitioning of probes between nanoparticles and the bulk aqueous phase, and the potential presence of a fraction of free and fast-moving probes in the solution does not perturb the study of large labeled nanoparticles [84].

There is one more difference between DLS and FCS results. DLS provides the z-average *D*, which is strongly affected by the presence of small amounts of large and strongly scattering species such as microgels, micellar aggregates, etc. In some cases, the scattering can be dominated by traces of such strong scatters, and information on 90–95 wt% of the polymer material of interest is lost. In contrast to DLS, FCS yields the number average characteristics, which are equally affected by particles of all sizes and reflect their number fractions.

In our recent studies, we focused on several complicating factors arising in studies of nanoparticles of a non-negligible size (e.g., polymeric micelles, vesicles) that can carry several fluorescent labels. When the dimensions of such particles become comparable to the typical dimensions of the effective volume (ω_1, ω_2), the correlated motion of the fluorophores located on a single particle affects the shape of the autocorrelation function. Recently, an approximate expression for the FCS autocorrelation function of diffusing particles of finite size has been derived by Wu et al. [85]. They have shown that the autocorrelation function of uniformly labeled spherical particles can be expressed in a form similar to (12) where the diffusion time, concentration, and dimensions of the active volume are replaced by corresponding apparent quantities that depend on the particle size. Qualitatively, the same results were obtained in our computer simulations, which are discussed later (see Sect. 4.3).

Another contribution to the correlation function, which cannot be neglected for large particles, is their rotational motion. This problem has not been treated theoretically so far but intuitively one can expect that when a large particle rotates, the mean-square displacement of embedded flurophores would be larger than that without rotation. Hence, a higher apparent diffusion coefficient than that for a pure translational diffusion should be observed. Recently, we also addressed this problem in our computer simulations. Because the use of FCS in polymer science is very limited, we will describe its advantageous features in Sect. 3.5.

3 Fluorescence Studies of Self-Organizing Polymer Systems

3.1 Brief Introductory Remarks

In this section, we will outline our work [84, 86–98] performed either within (or strongly related to) the POLYAMPHI network. We selected four typical examples that show (a) application of different variants of TRFS and (b) their high research potential. We describe the motivation and strategy of each study, summarize the most important observations obtained by a combination of several experimental techniques underlining the results of fluorescence methods, and discuss their specific advantages. Finally, computer simulations aimed at the support and elucidation of the complex behavior are outlined (Sect. 4).

The first study [86] concerns the conformational transition of polyelectrolyte (PE) chains in aqueous solutions with pH. The only used experimental technique was time-resolved fluorescence anisotropy. The experimental work suggesting the formation of "supercoiled" globular structures within poly(methacrylic acid) (PMA) chains with decreasing degree of ionization was done before the publication of the highly recognized paper by Dobrynin, Rubinstein and Obukhov [99] and before our participation in POLYAMPHI. However, thanks to the advances in computer technology and the methodology of computer simulations, we were recently able to support our earlier conclusions, made on the basis of fluorescence study, by molecular dynamics (MD) simulations [87] (described in Sect. 4).

The second example concerns the multidisciplinary study of the micellizing block copolymer polystyrene-*b*-poly(2-vinylpyridine)-*b*-poly(ethylene oxide) (PS–PVP–PEO), which shows a high tendency to aggregation and the formation of micellar clusters [88, 89]. It shows the application of SRM for studying the mobility and structural details of different domains in micelle-like polymeric nanoparticles. The fluorescence technique reveals interesting features of studied systems that are hardly accessible by other techniques. Section 3.3 is devoted to the development of the methodology of the solvent relaxation technique for studying nanostructured self-assembling systems.

The third example concerns a series of our LS and fluorescence studies on the structure and dynamics of micellar shells formed by weak PEs [90, 91] and the effects caused by the hydrophobic modification of shell-forming blocks [92–96].

The knowledge of changes in the shell structure due to hydrophobic modification of micelles is very important for their application as vessels in targeted drug delivery systems. In commonly designed systems, a small number of targeting groups are attached at the ends of shell-forming chains. The targeting groups are usually quite large and complex structures and may have an amphiphilic character due to the presence of one or more hydrophobic domains. When attached to micelles, they could try to avoid the polar aqueous medium and bury partially in the shell, which would decrease the targeting efficiency. To address this problem, we performed studies of model micellar systems tagged by small, but strongly hydrophobic, fluorophores. The experimental study employed a combination of time-resolved fluorescence measurement of the nonradiative energy transfer with LS techniques and the data were interpreted with help of Monte Carlo (MC) computer simulations.

The last example is meant as a sort of advertisement of FCS in polymer research [84, 90, 97, 98]. This experimental technique is very popular in biochemical and biological research, but is only little used in polymer science.

3.2 *Conformational Transition in Weak Polyelectrolyte Systems Studied by Fluorescence Anisotropy*

3.2.1 Motivation

Weak PEs contain ionizable groups in their chains that can dissociate in polar solvents, leaving electric charges on the chain and producing small mobile counterions that can escape into the bulk solvent. In contrast to strong PEs, where the positions and the number of the charged groups on the chain is determined by the synthesis and are independent of external conditions (pH, ionic strength, etc.), the dissociation of weak PEs depends on pH, ionic strength and other parameters of the system. Under equilibrium conditions, the charges appear and disappear at different positions on the chain via reversible dissociation/association processes with a fairly high frequency. Hence, the distribution of charges is an “annealed variable” in contrast to strong PEs, where it is “quenched”. This is why strong and weak PEs are also called “quenched” and “annealed” polyelectrolytes, respectively. Due to the high importance of PEs, their solutions and melts have been studied for a long time by a number of teams of experimentalists and theoreticians, and also by computer simulations [100]. The number of published studies is so vast that it is futile to give all relevant references. In the following text, we include only references to recent review articles and to the most important seminal studies relevant for the studied topic.

Because the understanding of the behavior of quenched PEs in solutions is much better than that of annealed PEs, first we will briefly summarize the most important conclusions concerning quenched PEs to show common features and then extend the discussion to weak PEs. It was realized relatively early that a sparsely ionized PE chain forms a compact globular conformation in a poor solvent whereas the conformation of the chemically similar, but highly ionized polymer is much more expanded. Hence, the solvent quality for a PE not only depends on the polymer, solvent, and temperature but also on the degree of ionization. A poor solvent for a neutral chain can be a good solvent for the same polymer when it is charged. The first theoretical attempt to treat the quenched PE chain in poor solvent was made by Khokhlov [101]. He showed that a spherically symmetrical globular globular conformation deforms in a prolate ellipsoid (almost a cylinder) with increasing charge. More detailed (nowadays generally accepted) description is provided by the paper by Rubinstein, and Obukhov [99]. The article predicts the formation of "pearl necklace" structures as a series of collapsed parts of the chain (globules, pearls) interconnected by stretched parts of the chain (strings). This inspired by earlier theoretical works by Kantor and Kardar [102], who explained the pearl necklace formation by physical arguments as used by Rayleigh in 1882 when he explained the instability of charged oil droplets [103]. The repulsion of electric charges tends to expand the droplet, but the interfacial energy tries to contract it. When a critical charge is reached, the droplet becomes unstable and splits in two smaller droplets, which move away from each other, thus minimizing the Gibbs energy. Analogous arguments explain the formation of "pearls" on the chain. In poor solvents, an attempt to minimize the number of unfavorable interactions between the polymer segments and solvent molecules leads to a compact globular conformation with minimum surface area. When the charge in the globule is such that the Rayleigh instability condition is fulfilled, it splits in two smaller globules. Because of chain connectivity, the daughter globules (pearls) are kept at a certain distance by a stretched part of the chain and cannot separate from each other. The above hypothesis was confirmed both by MC and MD simulations [104, 105] and at present, it is a generally accepted scheme of behavior of quenched PE chains.

In annealed PE chains, the situation is more complex. The probability of dissociation of a particular ionizable group depends, among other factors, on its distance from the nearest already ionized group. Hence, the distribution of charges may change in a cooperative manner with changing conformation. Therefore, it is not surprising that both theoretical and computer studies predict behavior that differs from that of quenched PEs. It was theoretically predicted by Raphael and Joanny [106] that an annealed PE in poor solvent should undergo the first-order transition from a highly charged expanded conformation to a collapsed conformation with very low ionization degree with a change in pH. Recently, it was shown by MC simulations in a semi-grand canonical ensemble [107, 108] that this behavior occurs deep in the poor solvent regime. However, in a mild poor solvent (close to θ-conditions), the transition proceeds via the necklace of pearls. A number of theoretical studies and MC simulations that have appeared recently support the above scheme. Most of these studies confirmed the possibility of the cascade transition via the pearl necklace structure only under conditions close to the θ-state. However, some controversy still exists because, e.g., Ulrich et al. [109, 110] found the necklace of pearl structure in very bad solvents at high degrees of ionization, and other authors, e.g., Borukhov et al. argued that the plateau on the titration curve does not have to be related to the sharp conformational transition [111].

PMA belongs to the most common and most important weak PEs. The behavior of its aqueous solutions has been a subject of numerous studies [112–118], which started in early 1950s with the paper by Katchalski [112]. The most important achievements were made by Strauss et al. [113–116], Morawetz et al. [117], and by Ghiggino et al. [118]. It was soon recognized that PMA differs from other PEs, e.g., from chemically similar poly(acrylic acid). In 1985, Ghiggino and Phillips [118] were the first to propose the “necklace of pearls” model specifically for PMA on the basis of indirect fluorescence studies, i.e., more than 10 years before a similar model by Dobrynin became popular and generally recognized (however, their paper is almost unknown).

3.2.2 Outline of Experimental Study and the Most Important Observations

As already mentioned, our experimental study [86] was inspired by the Ghiggino work [118] and by papers published by the Morawetz group [117]. The study was performed several years before the the Dobrynin paper [99] and was aimed at better understanding the conformational transition at that time called “hypercoiling” or “supercoiling”. We wanted to find our whether the transition proceeds as a cooperative sharp transition or as a progressive smooth process.

The strategy of the study was straightforward. A series of linear PMA samples differing in molar mass (M_w ca. 300,000) were synthesized and randomly tagged by pendant dansyl probes with degree of tagging below 1 mol%. Fluorescence lifetime and anisotropy measurements were performed in solutions differing in pH, ionic strength, and polymer concentration. The results were analyzed according to the model of Ghiggino and Phillips, and the working hypothesis that the supercoiling is a progressive process was tested. A dansyl moiety attached to the chain by a short flexible spacer (Fig. 5) is a suitable probe for this type of study. The position of the emission band does not depend on microenvironment polarity, but its quantum yield

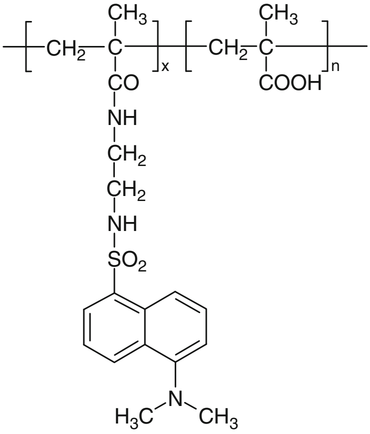

Fig. 5 The structure of dansyl-labeled PMA

Fig. 6 Typical dependence of (**a**) the fluorescence lifetimes $\tau_{F,1}$ and $\tau_{F,2}$ (*1* fast process, *2* slow process) and (**b**) relative amplitude of the fast process A_1 of the dansyl-labeled PMA on pH

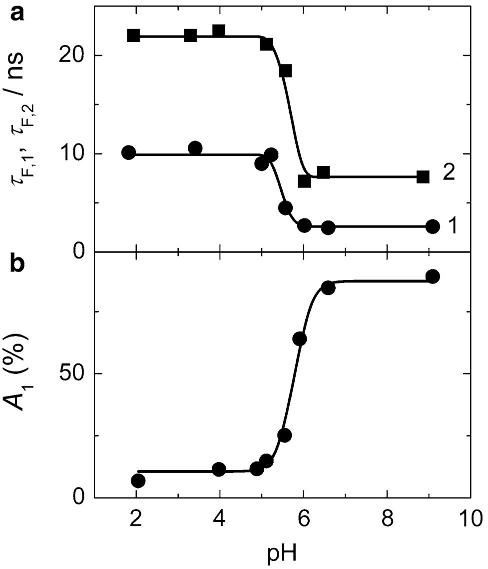

and fluorescence lifetime do. It is also a good probe for anisotropy measurements. The probes covalently attached to stretched parts of the chain (Fig. 5) are exposed to polar water molecules and can rotate fast, but those entrapped in nonpolar collapsed domains are considerably immobilized. It is evident that both the fluorescence and anisotropy decays monitor changes in chain conformation.

The most important results can be summarized as follows: The time-resolved fluorescence intensity decays measured in solutions of several PMA samples in a wide range of pH and ionic strength were always double-exponential. Both the short (units of nanosecond) and the long (tens of nanoseconds) fluorescence lifetimes increase with decreasing pH. Typical data are shown in Fig. 6a. The $\tau_{F,1}$ and $\tau_{F,2}$ dependences vs. pH (curves 1 and 2, respectively) exhibit a pronounced sigmoid shape, with the inflection point close to pH 5.5. The relative pre-exponential factor of the short-living fluorescence component, A_1, increases with increasing pH. The A_1 dependence on pH is depicted in Fig. 6b.

The obtained results can be explained as follows. In the pH region where the necklace of pearls structure exists, a fraction of probes are entrapped in compact globules and experience the nonpolar medium. The other probes attached to the stretched parts of the chains are exposed to polar water molecules. The probes are thus effectively distributed in two different microenvironments. The short lifetime corresponds to the water-exposed and the long one to the globule-embedded probes. The pre-exponential factors, when corrected by corresponding quantum yields, give the number fractions of both types of probes in the macroscopic ensemble. In the first approximation, the factors reflect the average numbers of monomer units in stretched and collapsed parts of the chain.

As the probe is more hydrophobic than the PMA monomer unit, we expect it induces a preferential collapse of the PMA chain in its vicinity. Nevertheless, the

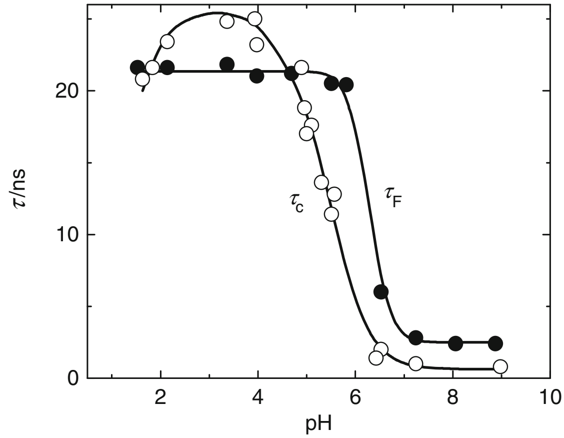

Fig. 7 Typical dependence of the mean rotation correlation time τ_c and the mean fluorescence lifetime τ_F of dansyl-labeled PMA on pH

measurements indicate that significant numbers of probes are exposed to water, even at low pH. A steep increase of fluorescence lifetimes and pre-exponential factor at around pH 5.5 suggests a sudden change in the microenvironment polarity of a considerable fraction of probes in a very narrow pH region.

Because of the complexity of the reorientation motion, we will discuss only the mean rotation correlation times, τ_c, even though the anisotropy decays indicate the presence of fast- and slowly rotating pendant probes. At high pH, the rotation correlation times are short (units of nanoseconds and less), but the residual anisotropy is non-negligible. It means that the rotation around single bonds of the spacer is fast, but reorientation does not proceed in all dimensions in the nanosecond time window. The τ_c dependence on pH is shown in Fig. 7. It is evident, that the reorientation slows down considerably with decreasing pH, but the change is quite gradual as compared with changes in mean fluorescence lifetime τ_F. The increasing values of the rotation correlation time reflect both (a) the locally restricted motion of the probe embedded in a collapsing part of the chain, and (b) rotation of the collapsed part of the chain around the axis defined by stretched parts connecting it with other globules (tens of nanoseconds are reasonable values for such a rotation). This type of "pseudo-one-dimensional" rotation of globules is supported by high residual anisotropy obtained at low pH.

A comparison of τ_F and τ_c vs. pH curves reveals interesting details: (a) curves in Fig. 7 differ in the steepness of the region close to their inflection points, and (b) onset of rising parts is shifted. Analysis of the above differences offers a deeper insight into behavior at the molecular level. The fluorescence lifetimes are sensitive to the polarity of the immediate microenvironment of the probe: when the chain starts to collapse at a certain pH, a small part of it reorganizes around the probe. Decreasing polarity hinders the dissociation of carboxylic groups in this domain and the interactions of the fluorophore with the microenvironment change suddenly (non-dissociated polymer units induce changes in the structure of water). The fluorescence lifetime is affected immediately and increases steeply with decreasing pH.

In contrast, the average rotation correlation time changes more slowly and we suppose that it better monitors the conformational behavior of PMA and shows gradual changes of chain conformations. A slow growth of τ_c is a result of a compromise between two effects: (a) the gradual increase in the mass of collapsing and fusing globules and (b) their increasing compactness. We believe that the comparison of τ_F and τ_c versus pH dependences supports the hypothesis that the conformational change is a gradual transition via the pearl necklace structures with pH. In the intermediate pH region, small globules grow and fuse with decreasing pH and simultaneously their density increases. At low pH, when only one compact globular conformation has been created, further decrease in pH promotes its compactness, which translates in its decreasing size and faster rotation. Hence the curve, which first rises with decreasing pH, drops appreciably in the low pH region.

The conclusions that we formulated in early 1990s are, in principle, in agreement with up-to-date knowledge. Water is a poor (but not too bad) solvent for non-ionized PMA and, hence, the conformational transition is expected to proceed not as a sharp transition, but via a cascade of pearl necklace structures. In Sect. 4.1, we will show that our recent MD simulations support the above description of the behavior. We included this almost-forgotten experimental study in the present feature article mainly because we returned to this problem and studied it theoretically within the POLYAMPHI network.

3.3 Solvent Relaxation Study of Self-Assembled Systems

3.3.1 Reversible Aggregation of Block Copolymer Micelles with PVP–PEO Shells in Acid Aqueous Solutions

Motivation

In a series of recent papers, we studied the copolymers containing PEO blocks [119–121]. PEO is biocompatible and easily soluble in aqueous media, and therefore it has been used as a shell of self-assembled biocompatible nanoparticles designed for targeted drug delivery [122]. The behavior of concentrated aqueous PEO solutions is fairly complex. It is influenced by the presence of a strongly hydrophobic (–CH_2CH_2–) group and hydrophilic (hydrogen-bonding) oxygen atom in its monomer unit. The amphiphilic character of PEO results in a strong aggregation tendency in some solvents. The presence of aggregated PEO chains in solutions has been proven by different experimental techniques, including light [123–127] and small-angle neutron scattering [128] and pulsed-field-gradient nuclear magnetic resonance (NMR) spectroscopy [125]. Even though various explanations of the aggregation mechanism (crystallization [123], inter-chain hydrogen bonding or the chain-ends effect [128], and subtle phase separation [129]) have been proposed, the exact origin of PEO aggregation under different conditions (PEO concentration, temperature, and also specific interactions with solvent molecules and other components) remains uncertain.

Some time ago, we investigated the behavior PEO-containing PE terpolymer PS–PVP–PEO in aqueous solutions [88, 89]. The micellization of this copolymer is strongly pH-dependent because PVP is protonized and therefore soluble in acidic solutions at pH lower than 4.8, but is deprotonized and therefore water-insoluble at higher pH. The PS–PVP–PEO micelle is a three-layer nanoparticle in which the PVP blocks form a middle layer between the rigid PS core and the PEO shell. The PVP layer is either collapsed at high pH, so that PS–PVP–PEO micelles resemble onion micelles formed in mixtures of PS–PVP and PVP–PEO diblock copolymers, or it is partially protonized, swollen, and flexible in acid aqueous media, so that the PVP layer becomes a soluble inner shell between the core and the outer PEO shell.

We found that the studied micelles containing long PEO chains, which should assure their solubility and thermodynamic stability, are surprisingly apt to a secondary aggregation and formation of micellar clusters. We suspected that the secondary aggregation of the PEO shell is caused by a hindered and incomplete solvation. Therefore, we supplemented the LS study of micellar solutions by SRM, with the aim of obtaining detailed information on the solvation of micellar shells.

Outline of Experimental Study and the Most Important Observations

The studied triblock copolymer PS–PVP–PEO was purchased from Polymer Source (Dorval, Canada). The number-average molar masses of PS, PVP, and PEO blocks were 2.1×10^4, 1.2×10^4, and 3.5×10^4 g mol^{-1}, respectively, and the polydispersity index of the sample was 1.10. The copolymer is insoluble in aqueous media, but the micelles can be prepared indirectly both in acidic and alkaline aqueous solutions by dialysis from 1,4-dioxane–methanol mixtures [88]. The micelles can be transferred from acidic to alkaline alkaline solutions and vice versa, but the addition of a base together with intense stirring promotes aggregation. Two factors contribute to the destabilization of micelles after the pH increase: (a) In alkaline media, the PVP blocks become insoluble, collapse and form an upper layer of the core. Since the cores of micelles are kinetically frozen, the association number does not change. The mass of insoluble cores increases, while the length of soluble shell-forming chains decreases, which results in a deteriorated thermodynamic stability of micellar solutions. (b) The PVP middle layer shrinks and PEO chains come close to each other, which worsens the solubility due to insufficient solvation of PEO blocks.

The most surprising feature of the behavior of PS–PVP–PEO micelles with water-soluble PVP (protonized) and PEO blocks in acidic media is their aggregation in the region of low pH. Because it is a rather unexpected phenomenon, we studied it in more detail. The distributions of relaxation times obtained by DLS are bimodal (Fig. 8). Angular dependences (not shown) prove that both fast and slow relaxation modes correspond to diffusive processes. The intensity of the slow mode decreases with increasing pH and decreasing copolymer concentration. At very low copolymer and HCl concentrations, the slow mode disappears completely. The DLS measurements thus show that PS–PVP–PEO solutions contain two types

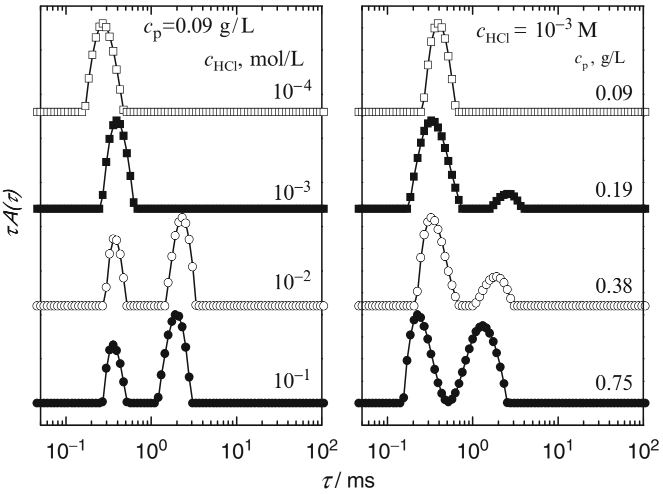

Fig. 8 Relaxation time distributions for PS–PVP–PEO solutions in HCl aqueous solutions, measured (*left*) at the copolymer concentration, c_p, of 0.09 g L^{-1} and HCl concentrations of 10^{-4}, 10^{-3}, 10^{-2} and 10^{-1} mol L^{-1}; and (*right*) in 10^{-3} M HCl, with copolymer concentrations of 0.09, 0.19, 0.38, and 0.75 g L^{-1}

Fig. 9 Hydrodynamic radius, R_H, of PS–PVP–PEO micelles in acidic aqueous solutions, as a function of pH

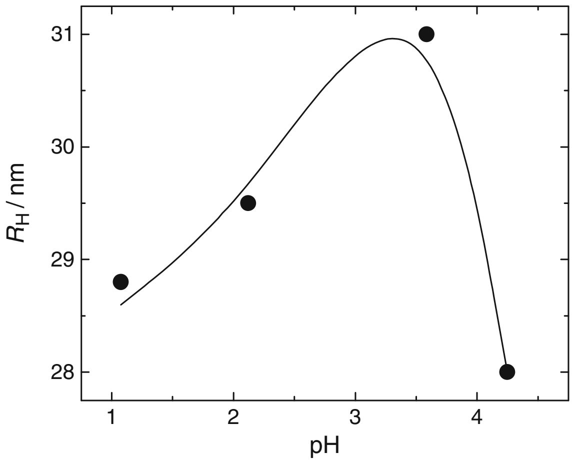

of particles and the balance between individual micelles and aggregates shifts in favor of aggregates with (a) increasing concentration of HCl and (b) increasing copolymer concentration.

A strong effect of electrostatic screening is evident from the dependence of the size of micelles on pH (Fig. 9). In the pH range above 3, the concentration of ions and the screening are negligible and R_H increases with decreasing pH due to substantial protonization of PVP blocks. The maximum R_H is reached at around pH 3. Below this pH value, a decrease in R_H is observed due to electrostatic screening by an increasing concentration of small ions.

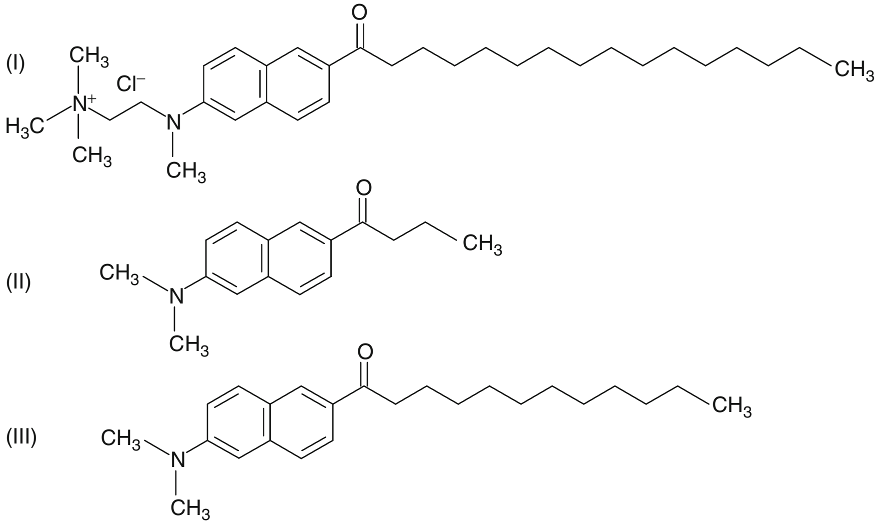

Fig. 10 Structures of (I) patman, (II) prodan, and (III) laurdan

Even though the aggregation of evenly charged micelles is a slightly surprising phenomenon, the effect of pH is an understandable result of electrostatic interactions. The addition of HCl supports the protonization of PVP blocks, but the H_3O^+ and Cl^- ions efficiently screen the electrostatic forces, which promotes the aggregation.

We performed the solvent relaxation study of acidic PS–PVP–PEO solutions with the aim of (a) proving the assumption that the formation of micellar clusters is a result of an insufficient solvation of PEO units, and (b) understandinghow the solvation is affected by pH and ionic strength.

First, we studied the solvent relaxation in solutions of diblock copolymer micelles. A commercially available polarity-sensitive probe, patman (Fig. 10, structure I), frequently used in phospolipid bilayer studies [123], was added to aqueous solutions of PS–PEO micelles. The probe binds strongly to micelles because its hydrophobic aliphatic chain has a strong affinity to the nonpolar PS core. The positively charged fluorescent headgroup is supposed to be located in the PEO shell close to the core–shell interface. The assumed localization has been supported by time-resolved anisotropy measurements.

The time-resolved emission spectra (TRES), $F_{\mathrm{TR}}(\nu,t)$, were reconstructed using the steady-state emission spectrum, $F(\nu)$, and the fluorescence decays, $I(\nu,t)$, measured at different wave numbers ν, according to the formula [130]:

$$F_{\mathrm{TR}}(\nu,t)=\frac{I(\nu,t)F(\nu)}{\int\limits_0^\infty I(\nu,t)\,\mathrm{d}t}. \tag{14}$$

For monitoring the relaxation process, we used two parameters of the time-resolved emission spectrum: (a) the full width in the half-maximum (fwhm) at the time t after excitation, $\delta(t)$, and (b) the correlation function, $C(t)$, corresponding to the normalized time-dependent Stokes shift [130]:

$$C(t) = \frac{\nu_{\max}(t) - \nu_{\max}(\infty)}{\nu_{\max}(0) - \nu_{\max}(\infty)}, \tag{15}$$

where $\nu_{\max}$(t) the wave number of the emission maximum at the time t after excitation. The value,$\nu_{\max}(0)$, corresponding to the energy level of the maximum disturbed system immediately upon excitation is not experimentally available but can be estimated by assuming that the initial Stokes shift corresponds to the difference of the absorption maxima between the studied polar solvent and a nonpolar reference solvent (hexane, etc.) [131]. For patman, which is charged and insoluble in nonpolar nonpolar solvents, we used spectra of an analogous compound, prodan (Fig. 10, structure II), because their spectra are almost identical in a large series of common solvents.

The comparison of the span of measured values with that based on the "time zero" estimation suggests that at least 70% of the reorientation motion has been displayed by monitoring the fluorescence behavior of micelle-embedded patman with our instrumental setup (time resolution). Figure 11 (curve 1) depicts the relaxation correlation function monitored by patman bound to diblock PS–PEO micelles.

Furthermore, we measured the time-dependent halfwidth of the emission spectra, which provides useful information on the extent of the studied process. It has been shown that the halfwidth should be constant in continuously relaxing homogeneous systems. In spatially inhomogeneous systems, the relaxation behavior proceeds differently. Because the properties of the system vary in space, individual fluorophores distributed in the system are nonequivalent and their solvent shells respond with different rates to the local electric field. This inhomogeneity gives rise to a new phenomenon that reflects the time distribution of phases of

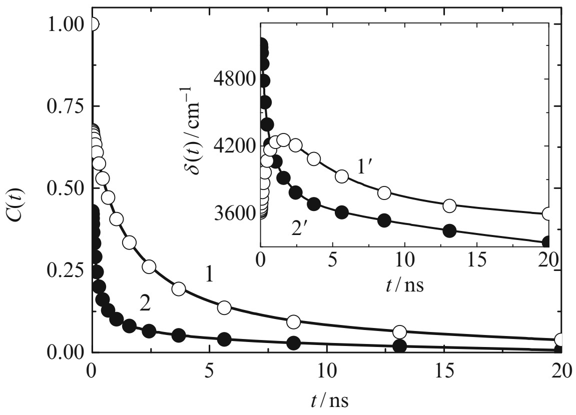

Fig. 11 Time-resolved Stokes shift, *C(t)*, of patman in PS–PEO micelles (*curve 1*) and PS–PVP micelles (*curve 2*). Inset: Time-dependent halfwidth of the time-resolved emission spectra of patman in PS–PEO micelles (*curve 1′*) and in PS–PVP micelles (*curve 2′*)

relaxations of individual solvation shells during the relaxation. The observed transient inhomogeneity increases significantly and the time-dependence of the observed halfwidth passes a pronounced maximum.

The time evolution of the halfwidth of the emission spectra provides information on whether the entire response, or just a part of it, was captured within the time-window of the experiment. If only a decrease is observed, the early part of the relaxation process is beyond the time resolution of the TCSPC equipment. By contrast, if only an increase is observed, the process is slow and the lifetime of the used fluorophore is not long enough for monitoring the overall relaxation process. The time evolution of the halfwidth is depicted in the inset in Fig. 11 (curve $1'$). The curve with a well-pronounced maximum supports the conclusion that the experimental setup detects ca. 70% of the total response, which we have drawn from the "time zero" frequency estimate. Therefore, we assume that a major part of the relaxation dynamics of bound water molecules engaged in the solvation sphere of PEO units occurs in the nanosecond time-range and can be monitored by time-resolved fluorescence measurement.

In order to get an idea of where the dye is located in the micelle, we performed time-resolved anisotropy measurements. The anisotropy of polarity-sensitive probes is not a good tool for monitoring the microviscosity because both the reorientation time and the residual anisotropy are influenced by solvent relaxation, and are thus wavelength-dependent [15]. Nevertheless, the measurements provides rough information on the viscosity of the microenvironment of the probe. The measurement of decay curves was performed at different wavelengths. All decays clearly showed high residual anisotropy (Fig. 12), indicating that the dye is localized in a constrained and considerably rigid domain close to the core–shell interface.

To support the conclusion on the patman location, the PS–PEO micelles were also labeled by laurdan, which has a shorter aliphatic chain and almost the same fluorescent headgroup, but it misses the permanent charge at the nitrogen atom. The measurement shows that the entire Stokes shift is small and the microenvironment relaxation is very slow, without any fast process beyond

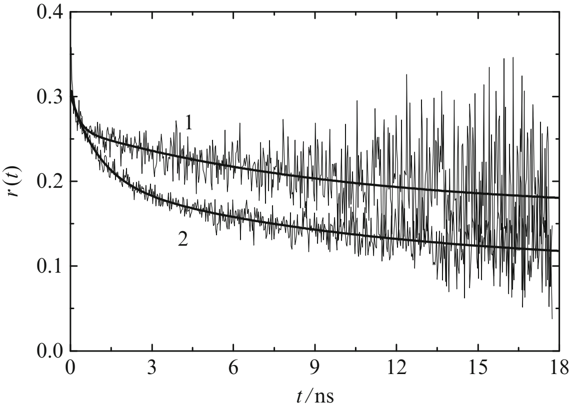

Fig. 12 Time-resolved anisotropy (experimental data and double exponential fits), *r(t)*, of patman in the PS–PEO micelles at emission wavelengths of 430 nm (*curve 1*) and 510 nm (*curve 2*)

experimental resolution. This indicates that the laurdan fluorescent headgroup is embedded in the PS core and that the aliphatic chain serves as an efficient anchor.

As we intended to study the pH-dependent hydration of PEO in triblock copolymer micelles, we measured the solvent relaxation for patman embedded in PS–PEO micelles both in acidic (0.01 M HCl) and alkaline (0.01 M NaOH) solutions for comparison. Because we found only marginal differences in the relaxation behavior, we can conclude that the dye itself does not exhibit any pH-dependent changes after binding to micelles and that the solvation of short PEO does not change much with pH (it is very important to emphasis that the PEO blocks are significantly shorter than those in the studied PS–PVP–PEO copolymer).

Consequently, the solvent relaxation was studied in PS–PVP micelles in 0.01 M HCl solution. The micelles are stable in acidic solution, where they are positively charged. Nevertheless, our earlier studies suggest that the PVP layer partially collapses around the core because PVP is only slightly protonized close to the nonpolar PS core [132]. A fairly high value of the residual anisotropy (around 0.2) measured at the maximum emission intensity (467 nm) suggests that patman is embedded in considerably rigid and little protonized domains close to the PS–PVP interface, which means that its location in PS–PVP micelles is similar to that in PS–PEO micelles.

The solvent relaxation in patman-labeled PS–PVP micelles is significantly faster than that in PS–PEO micelles. The shell-forming PVP chains are electrically charged and stretched at pH 2. A relatively open structure and low density of PVP shells assumes a considerable content of water and, therefore, an appreciable fraction of water molecules is not engaged in the solvation of PVP units. The fluorophore does not compete with PVP units for water molecules and the solvent reorganization is only weakly coupled with PVP segmental dynamics. The “time zero” estimation suggests that ca 60% of relaxation processes are beyond the experimental resolution. This conclusion is also supported by monitoring the fwhm that shows only the decrease (inset in Fig. 11, curve 2).

One can conclude that in both PS–PEO and PS–PVP micellar systems, the fluorescent surfactant patman is embedded in PEO-rich parts of the shell where the mobility of chains is strongly restricted. The differences in rates of the relaxation processes are mostly due to different solvation of the shell-forming chains and the different structure of water in the two types of shells. From the geometrical point of view, PEO chains are easily incorporated in the ice-like structure and the presence of both the hydrogen-bonding oxygen atom and the hydrophobic $-CH_2-$ group promotes the structure formation. The water-structure-supporting character of PEO is generally recognized and was confirmed by different experiments [133, 134]. The ice-like-structured water molecules bound to the concentrated and geometrically constrained (and hence only slightly mobile) PEO chains in the inner part of micellar shells are responsible for the slow relaxations in PS–PEO micelles.

After the study of reference diblock systems, the behavior of PS–PVP–PEO triblock was investigated in detail. For a correct interpretation of the pH effect on relaxation rates, the localization of the patman headgroup has to be known.

The following arguments support the assumption that it resides at the PVP–PEO interface and that pH changes do not cause hardly any displacements in the radial direction:

1. The hydrophobic chain tends to be buried in nonpolar parts of micellar structures (PS or non-protonized PVP), whereas the charged fluorophore headgroup prefers a polar environment.
2. At low pH, the swollen shell-forming PVP chains are partially protonized and we assume that the aliphatic chain of patman, which prefers the PS core to the partially protonized PVP, tries to pull the fluorophore closer to the core. However, the headgroup, which bears the same positive charge as the protonized PVP units, prefers the location in the PEO outer shell to the PVP middle shell due to electrostatic repulsion. Therefore, both effects roughly compensate each other and the location of patman hardly varies with pH. This assumption is supported by the experimental observation that in low pH solutions (below pH 4), both $C(t)$ and $\delta(t)$ show similar relaxation behavior as in PS–PEO micelles, which indicates the same microenvironment and supports the location of the headgroup in the PEO layer.
3. The time-resolved anisotropy measurements performed for pH 2 and 4 revealed fairly high values of the residual anisotropy (0.2 and 0.3, respectively), which indicates high rigidity of the microenvironment.
4. Fluorescence intensity measurements suggests that patman does not come to the immediate proximity of PVP segments: The patman fluorescence is quenched by deprotonized PVP chains. This was observed either in dioxane solution or in the alkaline solution of patman-labeled PVP–PEO micelles [89]. Becuase there is no observable decrease in fluorescence intensity for triblock copolymer micelles, it can be concluded that patman is not in direct contact with deprotonized PVP units.
5. Last, but not least, the measurements with increasing ionic strength of the solution at pH 2 did not show any effect on the solvent relaxation, which precludes significant displacement of patman in the radial direction from the interfacial region, either due to increasing protonization or to screening of electrostatic repulsion (at higher salt concentrations).

The correlation curves, as well as the shape of the time-dependent halfwidth, clearly suggest that the average mobility of the solvent molecules around patman decreases with increasing pH (Fig. 13). Although for pH 2–3, the limiting factor is the time-resolution of the instrumental setup, at pH 4, the relaxation processes is slow and its study is limited by the lifetime of the dye. We observe that the fast (experimentally unresolved) contribution decreases with increasing pH and that the nanosecond process, which is considered to be caused by the reorganization of bound water molecules engaged in the solvation sphere of PEO, prevails in the region of higher pH. At pH 4, we cannot monitor the end of the relaxation because the second contribution is too slow. The segmental motion and reorganization of the dehydrated polymer chains are assumed to be responsible for the slow relaxation, which exceeds the patman fluorescence lifetime.

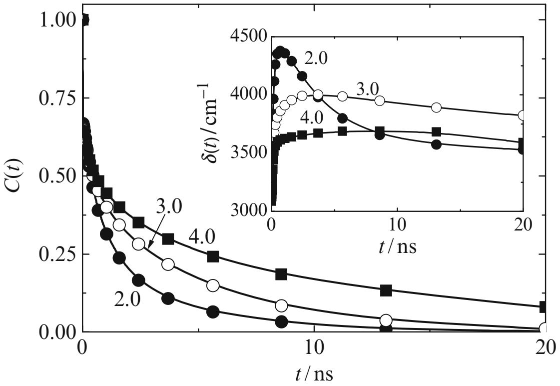

Fig. 13 Time-resolved Stokes shift, *C(t)*, of patman in PS–PVP–PEO micelles at pH values of 2, 3, and 4, as indicated on the corresponding curves. *Inset*: Time-dependent halfwidth, $\delta(t)$, of the time-resolved emission spectra of patman in PS–PVP–PEO micelles at different pH values, as indicated

The pH dependence of the solvent relaxation rate offers an explanation of the observed instability of micellar solutions at low pH and formation of a fraction of micellar clusters. The stability of micellar solutions assumes a proper solvation of PEO chains. However, PEO solvation promotes the ice-like structure and reduces entropy, which may cause solubility problems in systems with crowded PEO chains such as micellar shells formed by long PEO blocks. The addition of HCl (or other small ions) breaks the water structure, increasing the fraction of free and mobile water molecules, and reduces the fraction of PEO solvation-capable structured water molecules. Regarding the enthalpy-to-entropy interplay, the effect of increasing acidity resembles the effect of increasing temperature in the lower critical solution temperature (LCST) region. In both cases, the mobile solvent molecules would have to "condense" at the chain to assure its solubility and sacrifice considerable translational entropy. Regarding the LCST, the unfavorable entropy contribution increases with increasing temperature and at LCST, the phase separation occurs. In the studied case, the entropy contribution increases with the concentration of HCl: the mobile water molecules "liberated" due to the breakdown of the ice-like structure after the addition of small ions would have to form the structured solvation shell of PEO monomer units to provide sufficient thermodynamic stability of micelles in the solution. The complex entropy-to-enthalpy balance shifts towards free water molecules with decreasing pH, which promotes the formation of micellar clusters and minimizes the fraction of water molecules engaged in solvation shells.

The relaxation behavior at pH 1 is very interesting, but we could not analyze it because the time-resolved emission bands were bimodal. We studied the possibility of analyzing complex time-resolved spectra and in our recent paper [135] we describe a successful method of decomposition and treatment of bimodal time-resolved spectra. We used two probes with the same fluorescent headgroup differing in the length of the aliphatic tail. They have different affinity to micelles that allows study of their partitioning between micelles and bulk solvent. A detailed description and extended discussion exceeds, unfortunately, the scope of this paper, but we not only succeeded in treating the two time-resolved contributions (from free and micelle-solubilized probes) separately, but we also identified a slow contribution due to the motion of the probe with respect to micelle upon excitation. Because the solvent relaxation processes are very specific and complex, we have not yet attempted to perform the corresponding computer simulations.

3.4 Study of Shell-Forming Chain Conformations by Nonradiative Energy Transfer

3.4.1 Studies of Reference Systems of Nonmodified Weak Polyelectrolyte Shells in Solutions with Low Ionic Strength

Motivation

The properties of PE micelles in aqueous solutions are determined by the behavior of micellar shells, which can be regarded as convex PE brushes. Depending on the degree of charging and ionic strength, the PE brush can undergo several patterns of behavior. In systems where the density of charge on the PE chains is high, the electrostatic force acting on counterions is strong and prevents their escape in bulk solvent, which means that the brush remains electrically neutral. At low ionic strength, the osmotic pressure is high and individual brush-forming chains are strongly stretched. The brush is swollen and obeys the osmotic regime. In solutions with high ionic strength, the excess of small ions screens electrostatic interactions and the brush collapses, obeying the salted brush regime. We have been systematically studying the behavior of both hydrophobically modified and unmodified PE shells by a combination of several experimental techniques. Even though we have been interested mainly in modified systems, which we studied using fluorescence techniques, first we had to study the corresponding unmodified micelles as reference systems for comparison.

Outline of Experimental Studies and the Most Important Observations

The micelles were prepared by stepwise dialysis of diblock copolymer PS–PMA from mixed solvents to pure water. The copolymer contains one PS and one PMA block with an almost identical number of monomeric units (about 200). Further experimental details and copolymer characterization are given in [90]. Micelles were characterized by static light scattering (SLS) and DLS. The Zimm plot of experimental data in a borate buffer is regular and we used it for the evaluation of the weight average molar mass (M_{w}) of micelles and their radius of gyration. The scattering functions depend almost linearly on q^2 (scattering vector), which indicates that the micelles interact weakly with each other and that their interaction can be described by the excluded volume effect only. The monodisperese spherical micelles were further visualized by atomic force microscopy after their deposition on a fresh mica surface [90].

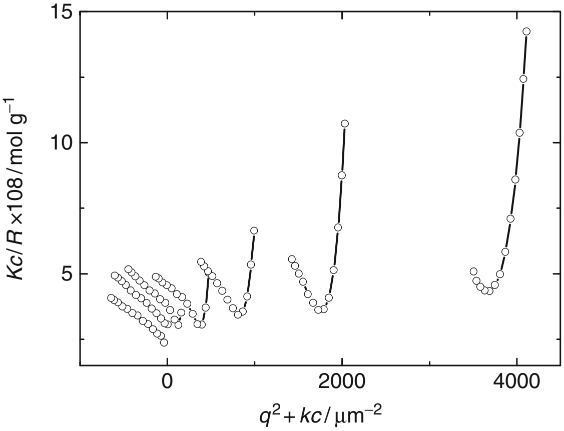

Fig. 14 Zimm plot of PS–PMA micelles in pure water (concentration range: 2.5×10^{-3} to $2.0\ \text{g L}^{-1}$)

The Zimm plot of micelles in a solution with extremely low ionic strength, which was prepared by repeated dialysis against an excess of deionized water in plastic flasks to prevent an alkaline ions release from glass, is shown in Fig. 14. At medium concentrations, one can observe an enormous deviation from the regular (linear) behavior. The dependences exhibit minima at q values that change with concentration. Such type of behavior is due to spatial correlations between individual micelles and is typical for strongly interacting systems. Because the irregular shape is observed at concentrations at which the average distances between micelles exceed 10–20 times their diameter, it suggests that structural correlations of scatters and the observed destructive interference of the scattered light at non-zero angles is due to long range electrostatic forces between significantly charged micelles.

We can conclude that that the “charged osmotic brush” regime, in which counterions escape into bulk solvent, can be observed when the experiments are performed in solutions with pH close to pK_A at very low ionic strength. Because our study provided the very first indirect evidence of behavior of PE micelles that, at that time, was only hypothetical and highly doubted by recognized theoreticians, we were looking for independent support and performed an MC study (see Sect. 4.2).

3.4.2 Nonradiative Energy Transfer Study of Conformations of Hydrophobically Modified Shell-Forming PMA Chains

Motivation

Many systems based on water-soluble block copolymer micelles have been developed and studied as vehicles for targeted drug delivery [122, 136, 137]. A typical copolymer suitable for such applications should fulfill several conditions: biocompatibility, biodegradability, and the ability to form hydrophobic domains that are capable of solubilizing and delivering hydrophobic drugs. The nanoparticles for an efficient targeted delivery have to bear targeting (recognition) groups at their periphery. They are usually chemically attached to the shell-forming blocks [138–142]. The targeting groups are chemically complex structures and may have an amphiphilic or partially hydrophobic character that could influence the targeting effect. In other worlds, their interaction with water does not have to be favorable and they could try to escape from the energetically unfavorable aqueous surrounding at the micellar periphery and bury deep within the shell close to the hydrophobic core. When this happens, their disappearance from the uppermost part of the shell negatively affects the drug delivery efficiency.

We addressed the above problem by studying a system of modified PS–PMA micelles with long PMA blocks end-tagged by a strongly hydrophobic molecule in mixtures of water with organic solvents and in purely aqueous media where electrostatic effects dominate the behavior [93–96]. We used anthracene (An) as the end-attached hydrophobic group, which allowed for fluorescence study. When we started the study, it was not a priori clear what would happen when such slightly modified micelles were dispersed in aqueous media.

Outline of Experimental Study and the Most Important Observations

For the experimental study, we used two almost identical PS–PMA samples, very similar to those studied in the above-described study. The first sample contained one pendant naphthalene group (Np) in between PS and PMA blocks. The second sample was tagged by Np in the same way as the previous one, but also by one An at the end of the PMA block. The two fluorophores, Np and An, were chosen because they represent a suitable pair for NRET studies and they can be chemically attached to specific sites of the studied system [143].

Experimental results were obtained by two experimental techniques, LS and TRFS. When the micelles are formed, all attached Np molecules (potential excitation energy donors) are localized at the core–shell interface. The Np fluorescence quenching due to NRET is expected if some energy traps (An) come relatively close to Np, i.e., to distances shorter or comparable with the Förster radius, R_0 (for the Np–An pair, ca. 2.1 nm [144]). Hence, the NRET study should prove whether a fraction fraction of shell-embedded An could closely approach the core.

The time-resolved quenching of the Np emission due to Np-to-An energy transfer is shown in Fig. 15. Three transfer-affected fluorescence decays (measured in the double-tagged system) normalized by decays in the absence of traps (measured in the single-tagged system under identical conditions) are plotted as functions of time in solvents differing in polarity (1,4-dioxane/water mixtures). The broken-like curve obtained in water-rich media, consisting of a steeply decreasing part and a constant part with almost no smoothly curved part in between, can be neither explained nor fitted by assuming any type of a continuous monomodal distribution of Np–An distances [92, 95]. It suggests the existence of two types of Np donors, which are either very strongly affected by NRET, or fully unaffected. In a spherically symmetrical system in which all Np are uniformly distributed in a narrow spherical layer at the core–shell interface, the concept of two types of Np molecules looks strange.

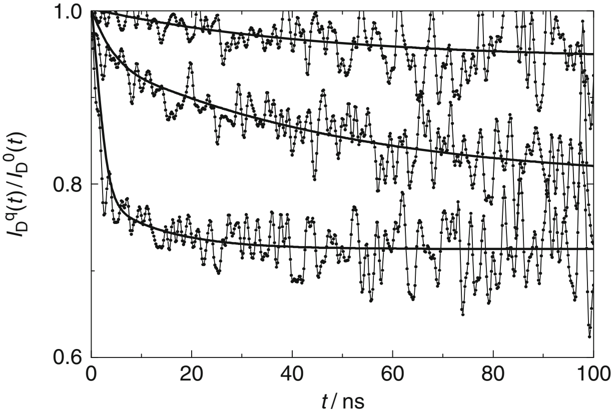

Fig. 15 Experimental kinetic NRET curves (Np-to-An energy transfer) of fluorescently labeled PS–PMA micelles in 5% water, 95% 1,4-dioxane (*top*); in 20% water, 80% 1,4-dioxane (*center*); and in water (*bottom*). Experimental data fitted by multiexponential functions

Fig. 16 Hydrophobically modified PS–PMA micelles with attached Np and An probes

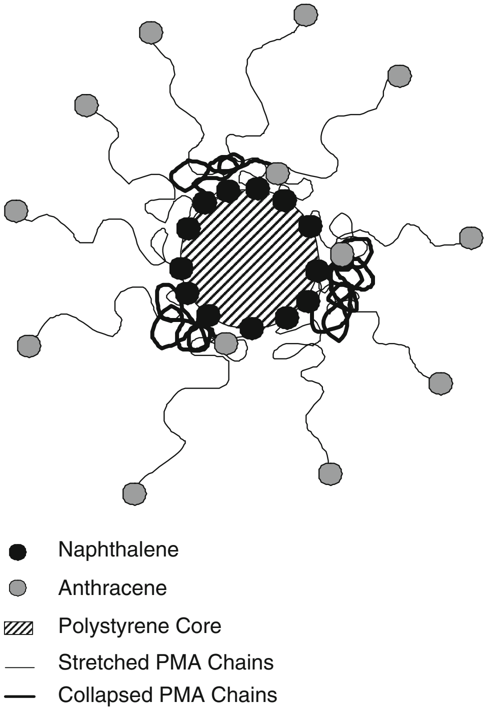

However, it can be rationalized when we postulate a rather specific conformational behavior of An-tagged shell-forming chains, which is depicted in Fig. 16.

The model assumes the coexistence of two distinctly different conformations created by identical shell-forming chains in each micelle under equilibrium conditions. The coexisting forms are (a) strongly collapsed and (b) stretched chains (see Fig. 16). Accepting the above scheme, it is obvious that some Np donors are affected by pendant An traps, which return in their immediate vicinity, while the other Np donors remain unaffected. Because in a typical fluorescence measurement, the fraction of excited fluorophores is less than 10^{-6}, a maximum of one Np per micelle is excited in the experimental study. Hence, the fluorescence decay from some micelles is very strongly quenched and that from others is unaffected by NRET, which leads to the "broken-like" time-resolved fluorescence response.

A pronounced bimodal distribution of chain conformations in a micelle that contains about 10^2 chains is something that one would hardly expect in an equilibrium system, even though bimodal distributions have been tentatively proposed for some other equilibrium polymer systems [145]. To elucidate the studied problem, we performed a series of simulations for modified micellar shells using the MC technique for neutral systems and the combined MC-mean field simulation. The simulations are described later (see Sect. 4.2).

3.5 Comparative Experimental FCS and DLS Study of Polymeric Nanoparticles

3.5.1 Motivation

For almost a decade, we have been using both DLS and FCS for studying various self-assembling polymer systems. We have developed a simple titration method for the evaluation of the number-average molar mass, M_n, of amphiphilic water-soluble nanoparticles. This method is very useful because the M_n of large particles is not easy accessible by common techniques such as osmotic pressure measurements, which lose precision for masses exceeding 10^5 g mol^{-1}. In the developed FCS method, an aqueous solution of the fluorescent surfactant with a strong affinity for polymeric nanoparticles and the self-quenched fluorescence (due to the formation of associates) is continuously added to the aqueous solution of nanoparticles. At relatively low fluorophore-to-nanoparticle ratios, ξ, single fluorophore molecules (which are no longer self-quenched) bind to different nanoparticles and the fraction of labeled fluorescent particles increases, which means that the particle number, $\langle N \rangle$, measured as the frequency of fluctuations, grows. When $\xi = 1$, each nanoparticle is on average labeled by one fluorescent probe (in reality, there is a Poisson distribution of the number of probes per one micelle) and the added probes start to bind to the already labeled polymer particles. If the size of nanoparticles is small enough, the frequency of fluctuations stops increasing and levels off, because the detector registers the double-labeled (or multiply-labeled) particle as one "point". The only difference is that some fluctuations are larger that the other. The experimental frequency as a function of the added amount of the probe consists of a linearly increasing and a constant part. The crossing point yields the number concentration of nanoparticles and the M_n. Very soon, we observed that the method gives good results for small nanoparticles (R_H ca. 10–30 nm, M_n ca. 10^5–10^7 g mol^{-1}), but it strongly underestimates molar masses of large nanoparticles (R_H higher than 50 nm). Because the M_n evaluation is very simple and does not require fitting the correlation curve, the analysis of discrepancies is straightforward and shows that the multiple labeling of large particles causes a higher frequency of fluctuations than that corresponding to the correct particle number. A careful comparison of results of both methods (based on autocorrelation functions) shows that they agree reasonably well for small and monodisperse particles, whereas for large particles, FCS yields very low values for $\langle R_H^{-1} \rangle_n^{-1}$ in comparison with the LS data and that the different polydispersity-affected averaging procedures cannot explain the observed differences. Therefore, we decided to perform a systematic comparative study devoted to the solution of the above open questions. In Sect. 3.5.2, we present some unpublished preliminary data on that topic.

3.5.2 Outline of Experimental Studies

In several of our papers [84, 90, 97, 98], we describe the characterization of various amphiphilic block copolymer micelles by FCS. The amphiphilic fluorophore octadecyl rhodamine B (ORB, Fig. 17) was used as a fluorescent marker for the micelles. ORB is suitable for labeling the micelles because it has a very low intersystem-crossing rate, which makes it highly resistant to photobleaching. Moreover, the contribution of the free probe emission to the signal is typically lower than 10% under the used experimental conditions because (a) free ORB in aqueous solutions forms self-quenched aggregates with a low fluorescence quantum yield, and (b) ORB is sparingly soluble in water and has a high binding affinity to amphiphilic block copolymer micelles in aqueous media. Using time-resolved fluorescence measurements, the partition coefficient, K, between PS–PMA micelles and bulk aqueous solution was found to be 1.5×10^5 [84].

In the experiments described below, FCS measurements were performed for varying concentrations of ORB added to the studied solution of micelles. The obtained autocorrelation curves were fitted to the function, assuming the presence of two types of fluorescent particles (free probe and labeled micelles) characterized

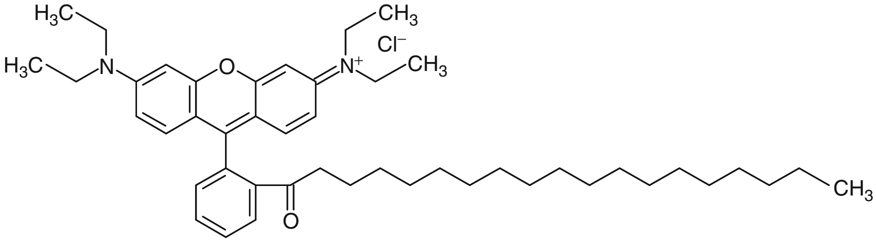

Fig. 17 Octadecyl rhodamine B

by diffusion times $\tau_{\mathrm{D},1}$ and $\tau_{\mathrm{D},2}$, absorption cross-sections σ_1 and σ_2, and fluorescence quantum yields q_1 and q_2:

$$G(\tau) = 1 + \frac{1 - \Phi(1 - \mathrm{e}^{-\tau/\tau_{\mathrm{C}}})}{\langle N \rangle (1 - \Phi)} \sum_{=1}^{2} Y_i \sigma_i^2 q_i^2 \left(1 + \frac{\tau}{\tau_{\mathrm{D},i}}\right)^{-1} \left[1 + \left(\frac{\omega_1}{\omega_2}\right)^2 \frac{\tau}{\tau_{\mathrm{D},i}}\right]^{-1/2}, \tag{16}$$

where $\langle N \rangle$ is the particle number, Φ is the fraction of molecules converted to the triplet state and τ_{C} is the characteristic time for the transition (τ_{C}^{-1} is the transition rate), Y_1 and Y_2 are the molar fractions of the two types of particles, and ω_1/ω_2 has the same meaning as in (12). It is necessary to point out that the simple model assumes only diffusive motions of point-like particles and does not account for photon correlations caused by rotational motion of the micelles or by multiple labeling, which will strongly affect the behavior of large particles (R_{H} exceeding 50 nm) in the FCS experiment.

Figure 18 shows a typical dependence of the particle number on the ORB concentration, c_{ORB} (the inset in Fig. 18 shows a typical FCS autocorrelation function). As explained in the previous section, the curve reaches the limiting value, $\langle N_{\mathrm{sat}} \rangle$, at the ORB concentrations at which virtually all micelles bear at least one ORB label. Provided that the effective volume, V_{eff}, is known from an independent calibration measurement based on the acquisition of $\langle N \rangle$ for a fluorescent dye solution of a known concentration, the M_{n} of micelles can be calculated using a simple relationship:

$$\langle M \rangle_{\mathrm{n}}^{\mathrm{FCS}} = \frac{c N_{\mathrm{A}}}{\langle N_{\mathrm{sat}} \rangle V_{\mathrm{eff}}}, \tag{17}$$

where c is the weight concentration of the copolymer and N_{A} is the Avogadro constant. The diffusion time of the labeled micelles, yields the number-average translational diffusion coefficient of the micelles, $\langle D \rangle_{\mathrm{n}} = \omega_1^2/4\tau_{\mathrm{D},2}$, from which the hydrodynamic radius, $\langle R_{\mathrm{H}}^{-1} \rangle_{\mathrm{n}}^{-1}$, can be calculated using the Stokes–Einstein formula.

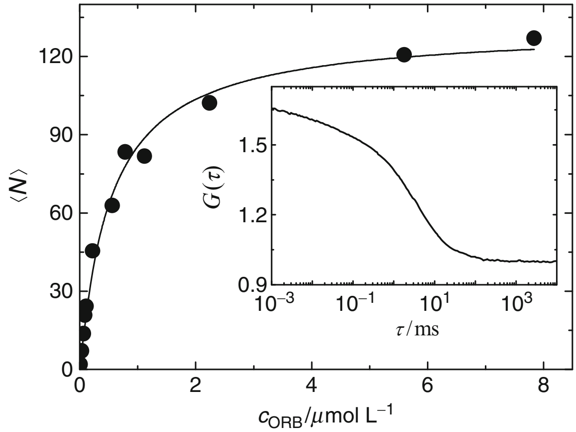

Fig. 18 Particle number, $\langle N \rangle$, as a function of the fluorescent probe concentration, c_{ORB}, for PS–PVP–PEO micelles in 0.01 M HCl. *Inset*: Typical correlation curve for an FCS measurement of ORB-labeled PS–PVP–PEO micelles 0.01M HCl

Table 1 Molar masses and hydrodynamic radii of several micellar systems, measured by light scattering and by FCS

Copolymer[a]	Solvent	$M_w \times 10^{-6}$ (g mol^{-1})[b]	$M_n \times 10^{-6}$ (g mol^{-1})[c]	$\langle R_H^{-1} \rangle_z^{-1}$ (nm)[b]	$\langle R_H^{-1} \rangle_n^{-1}$ (nm)[c]	Ref.
PS_{198}–PMA_{221}	0.05 M $Na_2B_4O_7$	8.0	4.7	54	42	[84]
PS_{136}–PVP_{117}–PEO_{795}	0.01 M HCl	2.7	0.5	37	28	[97]
PS_{136}–PVP_{117}–PEO_{795}	0.01 M NaOH	5.4	1.1	35	22	[97]
PS_{272}–PMA_{155}	0.01 M $Na_2B_4O_7$	3.0	2.3	30	–	[90]
PS_{29}/PVP^{d}_{217}	0.1 M HCl	0.8	0.5	32	28	[98]

[a] Subscripts denote degrees of polymerization of the blocks
[b] Measured by LS
[c] Measured by FCS
[d] Multiarm star copolymer with 20 PS_{29} and 20 PVP_{217} arms

Table 1 summarizes the molar masses and hydrodynamic radii of several amphiphilic block copolymer micelles obtained by FCS and LS measurements. Not surprisingly, values found by LS are larger due to the very high sensitivity of LS to larger particles (LS provides M_w and z-average provides the diffusion coefficients). A closer inspection of data and of experimental conditions is interesting, e.g., for PS–PVP–PEO micelles, the differences are very pronounced. One source of discrepancy is the different concentration ranges used in FCS and LS. As the FCS measurements were performed at lower concentrations, the differences reflect the secondary aggregation of PS–PVP–PEO micelles at higher concentrations, i.e., in the concentration range of LS measurements (units of g L^{-1}). Under experimental conditions of FCS measurements (polymer concentrations about 10^{-2} g L^{-1}), only individual micelles are present in the solution. Table 1 includes data for relatively small nanoparticles only. The effect of the size of studied nanoparticles has already been described in Sect. 3.5.1. To get better understanding of the effects caused by multiple labeling, etc., we performed a series of MC simulations (see Sect. 4.3).

4 Interpretations of Fluorescence Data with the Help of Computer Simulation

4.1 Interpretation of Time-Resolved Fluorescence Anisotropy Data by Molecular Dynamics Simulations

In a series of simulation papers, we used MD for studying the conformational behavior of linear and branched PEs. In one study, we addressed the time-resolved fluorescence anisotropy decays from fluorescently tagged weak PE chains in aqueous media, which we had experimentally studied earlier (see Sect. 3.2). We wanted to investigate and explore the relationship between the conformational behavior of the PE and the experimentally observable fluorescence anisotropy decays.

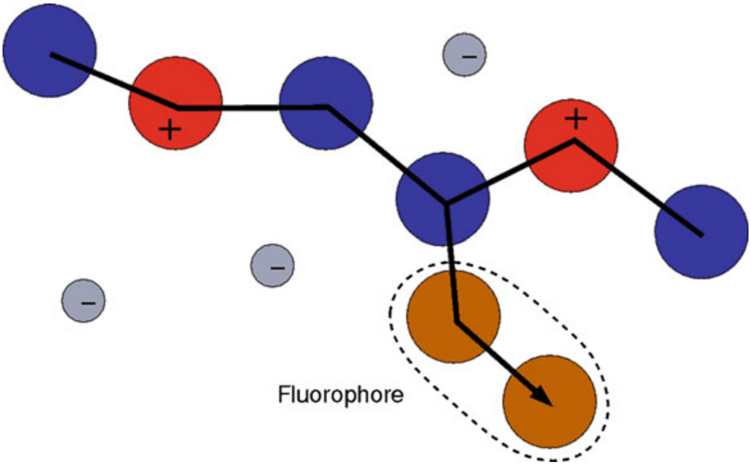

Fig. 19 Polymer model used in the simulations. *Red* uncharged monomer units, *blue* charged monomer units, *grey* counterions, *brown* fluorophore

4.1.1 The Model

In the simulation study of fluorescence anisotropy decay, a generic bead-spring model of the polymer was used. It is schematically shown in Fig. 19. Each bead can represent one or several monomer units in a real polymer. The degree of dissociation, α, is defined as the fraction of monomer units carrying electric charges. The interaction between monomer units of the polymer is modeled by the Lennard–Jones potential and the solvent quality is controlled by the depth of this potential, ε. As shown by Micka, Holm and Kremer, $\varepsilon \approx 0.34$ corresponds to the theta state [146]. The simulation study was performed for several values of $\varepsilon > 0.33$, i.e., under poor solvent conditions. The simulation technique used was MD coupled to a Langevin thermostat, i.e., the polymer was simulated in an implicit solvent. The counterions were simulated explicitly. A more detailed description of the polymer model can be found in the original paper [87].

The fluorophore was modeled by two beads that are attached as a short pendant side-chain (tag). Both the absorption and emission dipole moments of the fluorophore are defined by the direction of the tag (parallel), as indicated by the vector in Fig. 19, and the fluorescence anisotropy was calculated from its orientation autocorrelation function. For simplicity, we assumed that the reorientaional motion of the fluorophore is the only source of fluorescence depolarization. We neglected energy transfer and other processes that might occur in real systems. The fluorescence anisotropy decays were interpreted using the mean relaxation time, defined as:

$$\tau_{\text{mean}} = \frac{\sum\limits_i A_i \tau_i}{\sum\limits_i A_i} = \int\limits_0^\infty r(t)\mathrm{d}t. \tag{18}$$

There were two reasons for using the mean correlation time, τ_{mean}, rather than relaxation times of individual modes, τ_i: (a) experimental data were analyzed in the same way, (b) individual components, τ_i, reflect different types of the real motion, but they have no clear physical meaning in the coarse-grained model.

4.1.2 Conformational Behavior

Here, we summarize the patterns of conformational behavior that obviously affect the fluorescence anisotropy decay. For a detailed discussion we refer the reader to the original paper and references therein [87]. The conformational behavior of the polymer reproduced by simulations is in line with theoretical predictions [99] as well as other simulation works [104, 105]. The basic trends are depicted by a few snapshots in Fig. 20. With increasing degree of charging, the polymer undergoes the following conformations: a collapsed spherical conformation (Fig. 20a) deforms first in a prolate ellipsoid (Fig. 20b). At higher degrees of charging, it goes through a series of pearl-necklace structures with gradually increasing number of pearls (Fig. 20c). At high degrees of ionization, it ends up in an expanded conformation (Fig. 20d).

4.1.3 Comparison of Simulated and Experimental Data

The simulation study was aimed at the question of whether our intuitive interpretation of experimental fluorescence anisotropy data on PMA solutions was correct

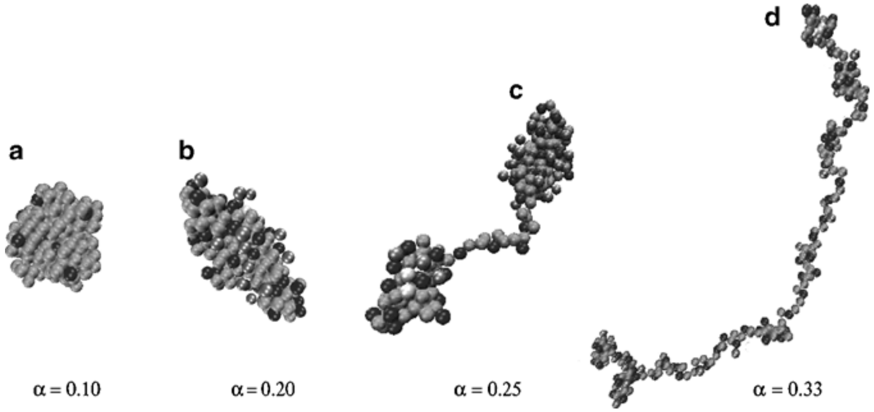

Fig. 20 Polyelectrolyte conformation as a function of the degree of dissociation (α). Simulation snapshots of the polymer with $\varepsilon = 1.3$, for several degrees of ionization: $\alpha = 0.06$ (**a**), $\alpha = 0.20$ (**b**), $\alpha = 0.25$ (**c**), and $\alpha = 0.33$ (**d**). Counterions not shown. For better visibility the snapshots differ in magnification; the real sizes of the monomer units are the same in all cases

or whether it needed revision. At the time our experimental study was performed, the nature of the PMA supercoiling process was not understood. A vivid discussion was focused on the question of whether the conformational change with pH is a cooperative (i.e., almost discontinuous) or progressive (continuous) process. It is fair to say that the present knowledge is still limited and there survives certain controversy concerning the interpretation by different research groups. Despite a number of later experimental and theoretical studies [104, 105, 107, 108, 147], the above question has not been unambiguously resolved until now. As mentioned above, theoretical studies by Raphael and Joanny [106] and recent MC simulations by Uyaver and Seidel [107, 108] indicate that a sudden sharp transition from a very compact globule to an almost fully stretched chain conformation occurs in really bad solvents, while in solvents of medium quality a gradual transition via the "necklace of pearls" takes place. Concerning PMA, water is a bad but certainly not too bad a solvent because the non-dissociated (i.e., uncharged) COOH is a hydrophilic group and almost neutral PMA is still reasonably soluble at low pH.

The comparison of simulation data with experimental data is shown in Fig. 21. It has to be noted that a strongly simplified polymer model was used and therefore only semiquantitative agreement was expected and achieved. The problem of mapping the simulation model onto a real polymer has been extensively discussed in the original paper [87]. The simulated and experimental orientational correlation times exhibit the same type of behavior, i.e., they progressively decrease with increasing degree of dissociation. The results of MD simulations thus support our intuitive interpretation of fluorescence experiments on PMA performed about two decades earlier.

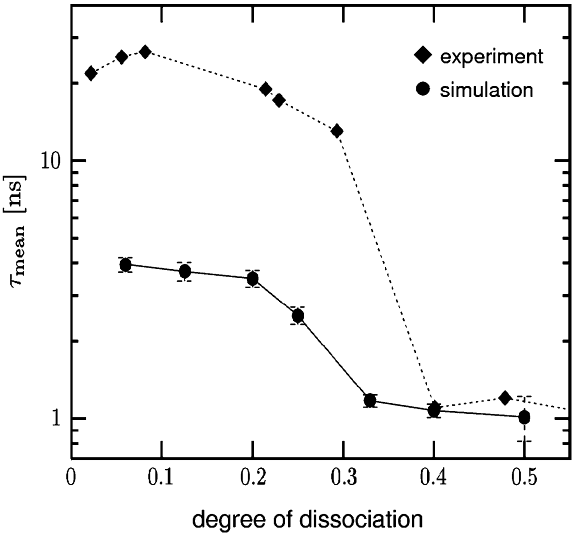

Fig. 21 Comparison of the experimental data (*diamonds*) and simulation (*circles*) of the mean characteristic decay time of the fluorescence anisotropy

4.1.4 Molecular Dynamics Simulations of Annealed Polyelectrolyte Chains

The main simplification of the above study can be summarized as follows: although the simulation was performed for a polymer with a fixed distribution of charges, it was compared to an experiment when the real PE was annealed, i.e. the charges on the polymer were not fixed but mobile. Therefore, we wanted to see to what extent the assumption of fixed charges affects the simulation. For this purpose, we simulated a polymer with mobile charges using essentially the same model as before [148]. The employed model for the mobile charges was simple, yet it captured certain essential features of the weak (annealed) PEs. The dissociation of the weak PE groups was modeled using a MC procedure. At a predetermined rate, the MD simulation was stopped, a random charged group on the chain was selected, and the charge was moved to a new position on the chain. The move was accepted using the standard Metropolis criterion [149]. In this way, the overall degree of charging of the polymer was kept constant while the distribution of charges along the polymer chain was allowed to vary.

The main result of the simulations was that the conformation of the polymer and distribution of charges along the chain are correlated. When the solvent for the polymer is not too poor, the charges are almost homogeneously distributed along the chain [148] and the probability of charging slightly increases close to the ends of the polymer. The inhomogeneity close to the ends is a consequence of lower charge density around the ends of the polymer. This intuitive result is in agreement with the simulation study of Limbach and Holm on end-effects on strong PEs [150].

A similar behavior was observed for PEs in poorer solvents when their degree of charging was high, as shown in Fig. 22. The simulation snapshot shows that

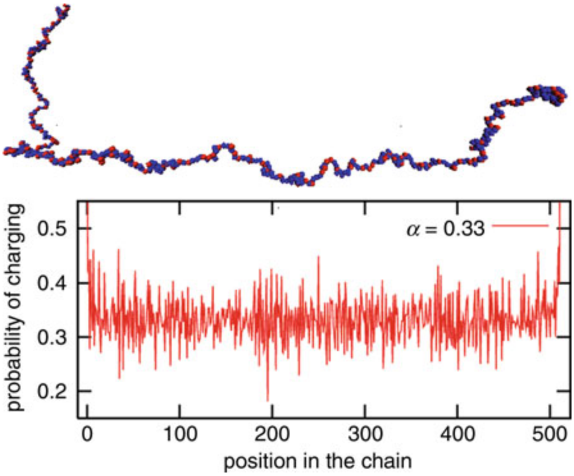

Fig. 22 The probability of charging of individual monomer units as a function of their position in the chain, in poor solvent for $\alpha = 0.33$ and $\varepsilon = m1.0$

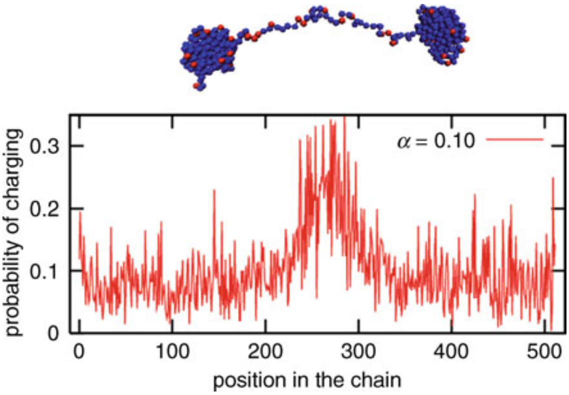

Fig. 23 The probability of charging of individual monomer units as a function of their position in the chain, in poor solvent for $\alpha = 0.1$ and $\varepsilon = 1.0$

the polymer conformation is expanded and that the plot of probability of charging of individual monomers as a function of their position in the backbone is homogeneous except for the ends, in accordance with the results for polymers in better solvents. However, when the degree of charging of such polymer is decreased so that the pearl-necklace conformation is formed, the situation changes dramatically. Figure 23 shows a simulation snapshot of such polymer and the plot of the probability of charging has a clear maximum in the central part that corresponds to the string connecting the pearls. This behavior can be understood when it is compared to the case of a polymer with fixed distribution of charges. In the latter case, when the pearl-necklaces are formed, there is a high density of charge inside pearls whereas the charge density in the strings is much lower. The strong (quenched) PE may respond by adopting the internal structure of the pearl so that the charged groups concentrate at its periphery, which has been observed in our simulation work on fluorescence anisotropy decays [87]. Besides this possibility, the weak PE has an option to transfer some portion of the charge from the pearls to the string and in this way to reduce the charge density in the pearls. This is exactly what is shown in the plot in Fig. 23. Hence, it could be concluded that the mobility of charges can serve as an additional mechanism for stabilizing the pearl-necklace structures in weak PEs as compared to the strong ones. Again, these results support the arguments for the formation of pearl-necklaces in weak PE systems. Yet, it has to be kept in mind that it is not the end of the puzzle. Some theoretical studies [106] predict a stepwise transition of weak PEs from a high degree of charging directly to a low degree of charging. In other words, they predict a forbidden range of degrees of ionization of a weak PE. In the light of these arguments, it would be desirable to work out a model in which the dissociation is explicit, i.e. the degree of dissociation is not fixed but comes out as a result of the simulation. This is the subject of currently running research projects and results may be expected in near future.

4.2 Monte Carlo Simulation of Shell-Forming Chain Conformations

4.2.1 Models and Simulation Techniques

In our computer studies of the conformational behavior of the shell-forming chains, we used MC simulations [91, 95] on a simple cubic lattice and studied the shell behavior of a single micelle only. Because we modeled the behavior of shells of kinetically frozen micelles, we simulated a spherical polymer brush tethered to the surface of a hydrophobic spherical core. The association number was taken from the experiment. The size of the core, lattice constant (i.e., the size of the "lattice Kuhn segment") and the effective chain length were recalculated from experimental values on the basis of the coarse graining parameterization [95].

The interactions are described by contact energies and the electrostatic energy. For contact energies we used the common matrix of interaction parameters in which the "reference interactions"(i.e., those where solvent is involved) are zero. The optimized parameters in units of kT are $\varepsilon_{\text{S-S}} = 0$, $\varepsilon_{\text{PMA-S}} = 0$, $\varepsilon_{\text{C-S}} = 0$, $\varepsilon_{\text{PMA-PMA}} = -0.27$, $\varepsilon_{\text{PMA-C}} = 0.8$, and $\varepsilon_{\text{C-C}} = 0.8$, where S, C and PMA stand for solvent (i.e., empty lattice site, occupied implicitly by solvent), C core (lattice point at the surface of the core or an attached hydrophobic pendant group), and the PMA bead (i.e., the Kuhn lattice segment, irrespectively of the ionization).

The electrostatic interactions (in aqueous solutions of annealed PEs, such as PMA, where the potentially ionizable groups get charged) are treated indirectly by solving the spherically symmetrical Poisson–Boltzmann equation (PBE) for the electrostatic potential $\varphi(r)$ [95]:

$$\frac{1}{r^2}\frac{\mathrm{d}}{\mathrm{d}r}\left[r^2\frac{\mathrm{d}\phi(r)}{\mathrm{d}r}\right] = -\frac{\rho(r)}{\varepsilon_0\varepsilon_\mathrm{r}}, \tag{19}$$

where ε_0 and ε_r are the dielectric vacuum permittivity and the relative (position dependent) permittivity of the dielectric medium, and the charge density $\rho(r)$ includes both the charge of the micelle (in the mean-field approximation) and of all small ions.

We consider the following components: –COOH, –COO$^-$, H_3O^+, OH$^-$, Na$^+$, and Cl$^-$, but not all are independent since they have to fulfill the relations, $K_\mathrm{w} = a_{\mathrm{H_3O^+}} \cdot a_{\mathrm{OH^-}}$ and $K_\mathrm{A} = \left(a_{\mathrm{H_3O^+}} \cdot a_{\mathrm{A^-}}\right)/a_{\mathrm{COOH}}$, where K_w and K_A are the ionization product of water and the effective dissociation constant describing the dissociation of carboxylic groups in PMA, respectively. The effective dissociation constant for PMA in solutions as a function of ionic strength and degree of ionization was measured by Morcellet et al. [151] and by Porasso et al. [152]. Nevertheless, we use the constant value $\mathrm{p}K_\mathrm{A} = 4.69$ for the monomeric methacrylic acid as a reasonable first approximation [153] because most theoretical calculations for PEs employs $\mathrm{p}K_\mathrm{A}$ for the monomeric unit, which facilitates the comparison with data of other authors on similar systems. The activities of components a_i are calculated using the Debye–Hückel limiting law [91]. The only independent parameters used in our simulations are pH and ionic strength, $I = (1/2)\ \Sigma c_i {z_i}^2$. The position-dependent concentrations of small ions are expressed according to the Boltzmann theorem as $c_i(r) = c_{i,\infty} \exp(-q_i z_i \varphi(r)/kT)$.

In summary, the computer simulation of micelles with shells formed by an annealed PE is a combination of MC with the self-consistent field treatment of electrostatic forces. However, it goes beyond the mean-field approximation. It is also evident from simulation snapshots (see below) that the a priori assumption of the spherical symmetry of the electrostatic field (which is an inherent feature of studied micelles) does not impose a strong constraint on instantaneous chain conformations.

4.2.2 Results and Discussion: Shell-Forming Chains at Low Ionic Strengths

We performed a series of coarse-grained lattice MC simulations for PE brushes tethered to spherical cores that mimic the studied micelles as close as possible. Details on the coarse-graining procedure can be found in [95]. MC simulations yield (a) snapshots of micellar structures and (b) a number of ensemble average characteristics, such as radius of gyration, R_G (as a function of pH and I) and its distribution, segment density profiles of the shell-forming blocks, ionization profiles, radial dependences of the electrostatic potential, etc. To give an idea of simulated structures, we show two snapshots that depict typical micelles at different pHs (pH 4 and 6, Figs. 24 and 25, respectively). A comparison of both snapshots shows increasing swelling of micellar shells with pH due to the well-known effect of ionization. The dependences of gyration radii on pH are shown in Fig. 26. The snapshots and rather trivial dependences of radii of gyration on pH have been included in order

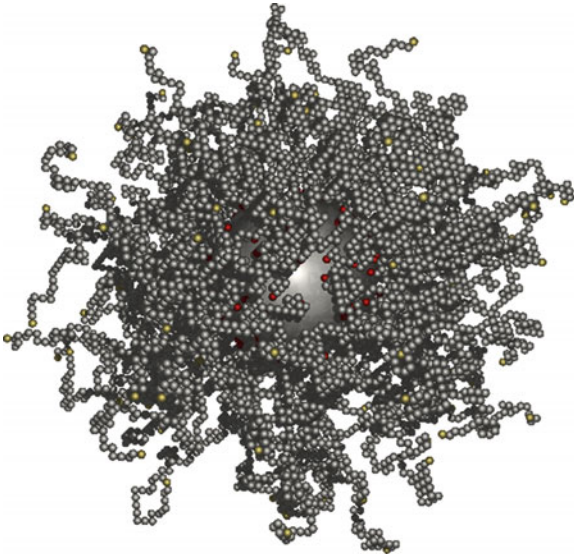

Fig. 24 Snapshot pf PS–PMA micelle at pH 4 and I 0.01

Fig. 25 Snapshot pf PS–PMA micelle at pH 6 and *I* 0.01

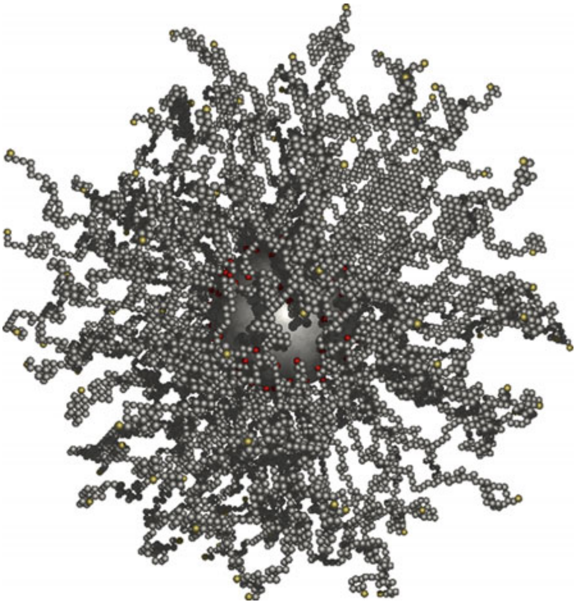

Fig. 26 Simulated dependence of R_G of PS–PMA micelles on pH for ionic strengths, *I*, of 0.01 and 0.01

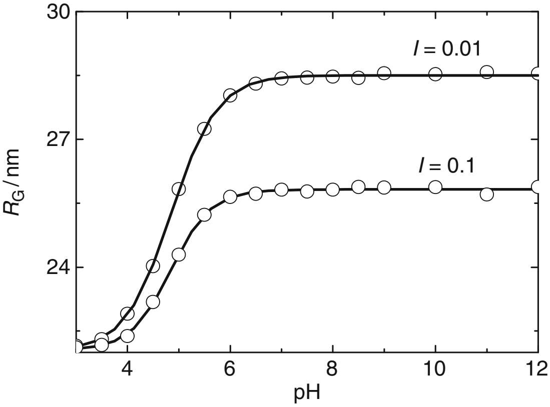

to document the basic correctness of the model and the simulation procedure used. We would like to point out that the pronounced coiling of the shell-forming chains at the micellar periphery, where the degree of dissociation and electrostatic interactions are important, demonstrates that the constraint imposed by the a priori assumed spherical symmetry of the electrostatic field is weak and does not artificially restrict the conformational behavior of individual chains.

Furthermore, we discuss data that are directly related to the PE behavior at low close to $\mathrm{p}K_\mathrm{A}$. Figure 27 shows the electrostatic potential as a function of the distance from the micellar center, *r* (the function related to the vertical scale on the right) and the *r*-dependent concentration profiles of the positive and negative charge

Fig. 27 Simulated concentration profile (*black circles* correspond to *left* axis) and electrostatic potential (*white circles* correspond to *right* axis) in PS–PMA micelles as a function of the distance from the micellar center for pH 5 and ionic strength 0.001

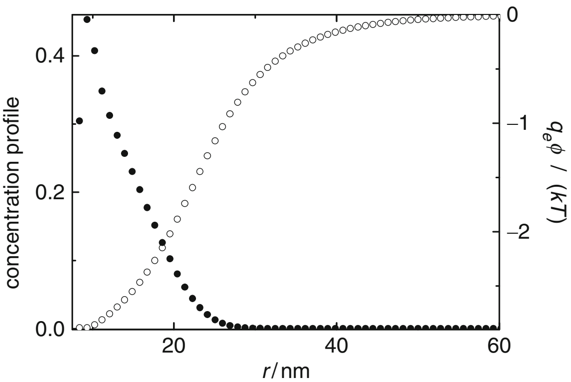

(corresponding to the vertical scale on the left) for the same condition, i.e., pH 5 and $I = 0.001$. It is evident that the electrostatic potential at the periphery of micelles is significantly negative and that there exists an excess of negative charge in the shell and an excess of positive charge around micelles.

4.2.3 Interpretation of NRET Data: Conformations of Hydrophobically Modified Chains

A pronounced bimodal distribution of chain conformations in a micelle that contains about 10^2 chains is something that one would hardly expect in an equilibrium system, even though bimodal distributions were earlier tentatively proposed for some other equilibrium polymer systems [145]. To elucidate the studied problem, we performed a series of simulations for modified micellar shells using the MC technique for neutral systems and the combined MC-mean field simulation technique for charged aqueous systems. Figure 28 compares the distributions of radial distances of end segments from the core (i.e., distances of An), $\rho_\mathrm{T}(r)$, in the modified and unmodified systems. Similar information can be obtained from the distribution function of random Np–An pair distances, $P_\mathrm{NA}(r_\mathrm{NA})$, i.e., the distribution of distances of An traps around a randomly excited Np donor, averaged over all donors in the modified micellar system, which allows for the calculation of fluorescence decays. Both functions are bimodal in the modified system (with a narrow peak in the region of small distances), which confirms our working hypothesis used for the above-outlined tentative interpretation of NRET results. The Np fluorescence decay can be calculated using the $P_\mathrm{NA}(r_\mathrm{NA})$ function; however, the MC method offers a more direct evaluation of its shape. The simulation yields a number of independent micelles and, for each equilibrated micelle, it is possible to solve numerically the master equation [92] describing the probability $p(t)$ that the excitation is located at time t at the fluorophore that was excited at time $t = 0$:

$$\frac{\mathrm{d}p(t)}{\mathrm{d}t} = -\left[\frac{1}{\tau_\mathrm{d}} + \sum_{i=1}^{n} k_\mathrm{T}(r_i)\right] p(t), \tag{20}$$

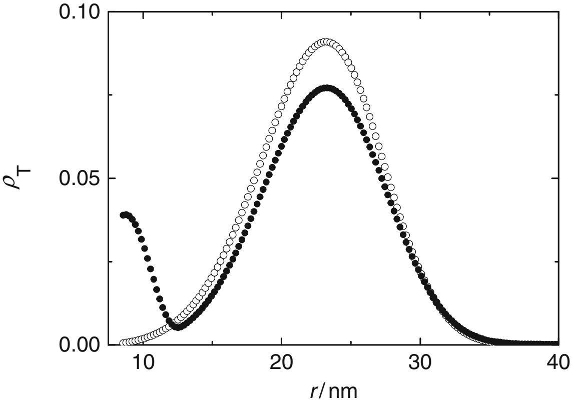

Fig. 28 Simulated distributions of radial distances of end segments from the core in hydrophobically modified (*black circles*) and unmodified (*white circles*) PS–PMA micelles

where τ_d is the natural (unaffected) fluorescence lifetime of the donor (Np) and $k_T(r_i)$ are the position-dependent rate transfer constants:

$$k_T(r_i) = \left(\frac{1}{\tau_d}\right)\left(\frac{R_0}{r_i}\right)^6, \tag{21}$$

describing the rate of NRET for individual pairs, i, formed by the randomly excited Np and all fixed An traps in one micelle. The first term of the right hand side (rhs) of (20) describes the depletion rate of the excited state by fluorescence, and the sum of $k_T(r_i)$ multiplied by p describes the net effect of NRET in system with a fixed position of all An. The averaging over different arrangements of traps around the excited donor (i.e., over all possible conformations of the shell-forming chains in the micellar system) yields the following formula for the enumeration of the experimentally accessible fluorescence decay:

$$I_d^q(t) = I_d^0(t)\left\langle \exp\left[-\sum_{i=1}^{n}\left(\frac{R_0}{r_i}\right)^6\left(\frac{t}{\tau_d}\right)\right]\right\rangle. \tag{22}$$

The comparison of experimental and calculated decays that is depicted in Fig. 29 shows a good quantitative agreement of both dependences.

To summarize the results of MC simulations, we can say that the computer study confirmed our hypothesis on the bimodal distribution of conformations of the modified shell-forming chains. The results are interesting both from the theoretical and practical points of view. Concerning the practical design of micelle-based systems with the end-attached targeting groups, the study indicates that the choice of a suitable group requires great care.

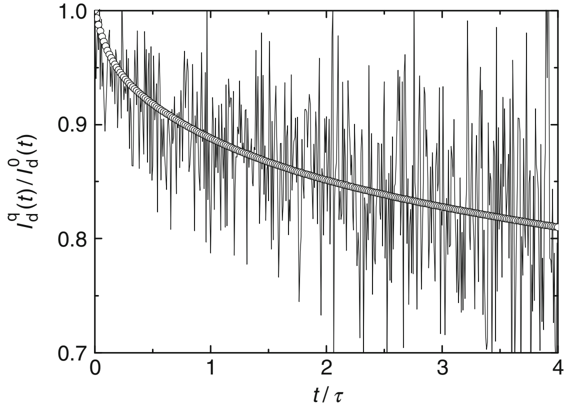

Fig. 29 Comparison of experimental curve (*noisy*) and simulated data (*circles*) describing the NRET kinetics of fluorescently labeled PS–PMA micelles

4.3 Monte Carlo Simulation of FCS Data

As mentioned in Sect. 2.5, we used computer simulations to address some problems that arise when FCS is used to study the diffusion of larger particles. In particular, we simulated how the FCS results are affected when large particles carry multiple labels and looked at how important is the effect of the rotational diffusion of such particles.

We used a simple simulation program that was developed in our laboratory. The program simulates an FCS experiment, i.e., it emulates the behavior of an ensemble of particles diffusing in a volume irradiated by a laser beam with a defined spatial intensity profile. The particles can be either point-like or finite-sized and they perform both translational and rotational diffusive motion. The probability of displacement in time Δt is drawn from the known probability distribution:

$$P(x,\Delta t) = \frac{1}{2}\sqrt{\pi D\Delta t}\exp\left(-\frac{x^2}{4D\Delta t}\right), \tag{23}$$

where x is the position of the particle, Δt is the time interval and D is the translational diffusion coefficient. Besides translational diffusive motion, the finite-sized objects can optionally perform rotational diffusion. Because the probability distribution for the rotational diffusion cannot be expressed in an analytical form, the rotational diffusion is simulated “by definition”, i.e., in the time interval Δt, each object is rotated n_{rot} times around random axes by an angle φ given by the expression:

$$\phi = \sqrt{\frac{6\Theta\Delta t}{n_{\mathrm{rot}}}}, \tag{24}$$

where Θ is the rotational diffusion coefficient, which is related to the translational diffusion coefficient, D, as:

$$\Theta = \frac{kT}{8\pi\eta R^3} = \frac{3D}{4R^2}, \tag{25}$$

where R is the radius of the particles, k is the Boltzmann constant, T is the temperature and η is the viscosity of the solvent. Each of the diffusing particles can carry several fluorescent labels distributed over its volume or on the surface. The number of emitted photons in the interval Δt is given by the Poisson distribution:

$$P_\nu(n) = \nu^n \frac{\mathrm{e}^{-\nu}}{n!}, \tag{26}$$

where ν is the expected mean number of successful results (number of photon emissions in our case). For a particle in position (x,y,z) we obtain ν as:

$$\nu = Q \Delta t\, E(x,y,z), \tag{27}$$

where $E(x,y,z)$ is the excitation profile defined by (10) and Q is the instrument constant. In a real system, Q comprises a number of factors such as detection efficiency and quantum yield. In the simulation, it is an adjustable parameter that influences the computational efficiency but has no effect on the results. The simulated system is in spherical boundary conditions so that when a particle diffuses out of the simulation cell, it is deleted and a new particle is generated at a random position on the surface of the cell. The boundary conditions perturb the correlations at longer times that may potentially cause problems. However, for a given size of the simulation cell, as well as other parameters of the simulated system, analytical expressions can be derived that estimate the expected systematic error. Moreover, this error can be made arbitrarily small by choosing a large enough system and simulating for long enough. On the other hand, a natural limitation is the acceptable computer time for one simulation. For practical purposes, we accept an error of up to 5% in the obtained diffusion coefficient and concentration, which is still better than can be obtained from experiments.

4.3.1 Simulation Results

We used the computer simulations to study the effect of the size of diffusing particles on the results obtained from the FCS measurements. The simulated particles were spheres that could carry one of more particles on their surface. The translational diffusion coefficient of the particles was calculated from (25) and was used as an input parameter. The obtained fluorescence intensity trace of the simulated system was processed to calculate the autocorrelation function $G(\tau)$ (11), which was then fitted using the analytical expression for point-like particles (12).

When the diffusing particles carry only one fluorescent label, the statistical characteristics of the diffusion of the labels exactly corresponds to that of point-like particles. Data points in Fig. 30 show the simulation data for particles carrying one label. The data are plotted using relative units: On the vertical axis, we plot the ratio of the apparent diffusion time (i.e., that obtained from the fit of the autocorrelation function) to the true diffusion time (i.e., that which was an input parameter of the simulation). On the horizontal axis, we plot the ratio of the particle radius, R, and

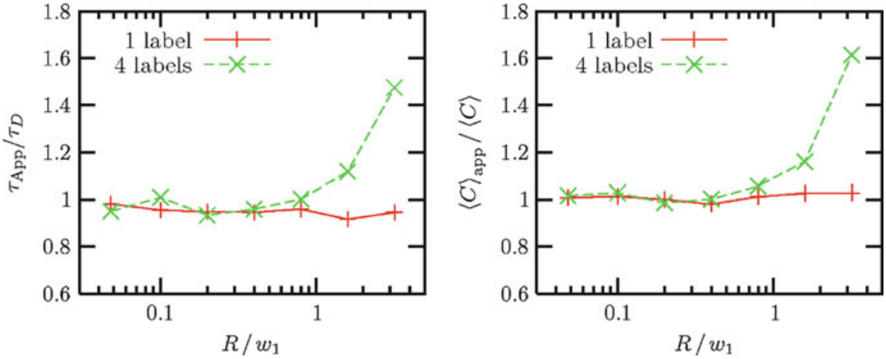

Fig. 30 Effect of multiple labeling on the apparent diffusion timesg τ_{App}, (*left*) and on the apparent concentration, $\langle C\rangle_{\text{App}}$ (*right*)

the typical dimension of the active volume, ω_1. Since the particles carrying one single label behave in the same way as point-like particles, in our set of units, we should obtain that the ratio $\tau_{\text{App}}/\tau_{\text{D}} = 1.0$. The deviations from this value characterize the intrinsic error of the simulation. As mentioned in previous paragraphs, we set up the simulated system so that the error should be up to 5%. Since these simulation data agree well with the theory, we used them as a reference set of data to which other results are compared. In the case of particles, which carry more fluorescent labels, there is an additional correlation between the motion of labels attached to the same particle, which is reflected in the autocorrelation function. When data from such simulation are fitted using (23), an apparent diffusion time is obtained, which should be significantly different from the translational diffusion time used as an input for the simulation. Figure 30 also shows the simulation results for particles carrying four labels. The data in the left graph of Fig. 30 show that when $R \ll \omega_1$, the apparent diffusion time does not significantly differ from the true value. On the other hand, when $R \approx \omega_1$, the apparent diffusion time significantly differs from the real value. This is in agreement with the theoretical predictions of Wu et al. [85]. A similar plot for the apparent concentration is shown is shown in the right graph of Fig. 30. Again, for point-like particles the single-label data points are very close to unity for any particle size while the four-label data points significantly deviate from the real values when $R \approx \omega_1$.

Another, yet unexplored, problem is the extent to which the autocorrelation function and the obtained diffusion characteristics are affected by the rotational diffusion of the particles. Intuitively, one can expect that the rotational diffusion effectively speeds up the decay of the autocorrelation function and hence shorter diffusion times should be observed. This is shown in Fig. 31. The one-label, no rotation data points are the same as in Fig. 30 and serve as a reference. The other data points show the same system in which the rotation of the diffusing particle is switched on. As could be expected, when the relative size of the particle is small as compared to the dimensions of the active volume, the rotation has little effect. However, when the particle dimensions are comparable to those of the active volume, the apparent diffusion time

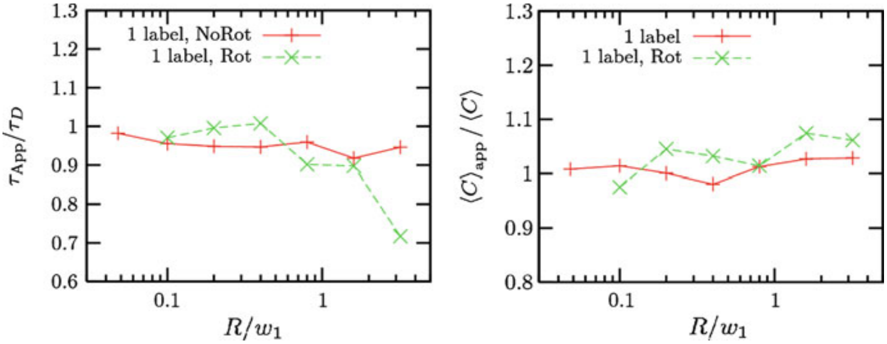

Fig. 31 Effect of rotation on the apparent diffusion time, τ_{App}, (*left*) on the apparent concentration, $\langle C\rangle_{\mathrm{App}}$ (*right*)

is significantly lower than the real one. When the rotational diffusion is switched on for particles that have more than one label (data not shown), the effect of rotation is much weaker. It can be understood by analyzing the extreme case: for a very high number of labels, the large particle is uniformly covered with fluorophores and it does not matter at all if it is rotating or not. Hence, with increasing number of fluorophores on the diffusing particle, the effect of rotation is gradually suppressed. Figure 31 shows that the effect of rotation on the apparent concentration is close to the intrinsic error of the method and hence can be considered as negligible.

To summarize the results of the MC simulations, we may say that when the diffusing particles have dimensions comparable to the dimensions of the effective illuminated volume, their size (and shape) strongly affects the autocorrelation function. If such system is treated using the standard model for point-like particles, the obtained apparent diffusion coefficients may significantly differ from the real ones. On the other hand, when the large particles also perform rotational diffusive motions, then the apparent diffusion times are affected in the opposite direction, as in the case of multiple labeling. The effect of rotational diffusion is important when there is only one label per particle, and with increasing number of fluorophores it diminishes. Both these effects should be taken into account when FCS is applied to study the diffusion of particles that have dimensions comparable to the dimensions of the illuminated volume. On a semi-quantitative basis, the simulation results explain the discrepancy between the diffusion coefficients (hydrodynamic radii) of large particles when measured by FCS and DLS.

5 Concluding Remarks

In this article, we have selected and reviewed several studies performed during (or closely connected to) our participation in the POLYAMPHI network with the aim of showing the high research potential of fluorescence techniques for investigating self-assembled stimuli-responsive polymer systems. The selection was based on three criteria.

First, we wanted to show interesting associative and conformational behavior of amphiphilic copolymer systems in aqueous media containing both neutral water-soluble (e.g., PEO) and weak PE blocks (e.g., PMA, PVP). On purpose, we omitted common types of straightforward studies that are currently performed by a number of groups (and also in our laboratory) and chose to focus on the specific features of their behavior and on their detailed investigation that could not have been done without specialized fluorescence techniques. One of goals was the demonstration that the structure of water and its changes due to the solvation of water-soluble chains plays an important role in self-assembling processes. In our studies, we often observe fairly unexpected behavior and witness how the intricate entropy-to-enthalpy balance influences the behavior of aqueous nanoparticle systems. In contrast to biochemists and biologists, who take great care over the role of water and talk about "hydrophobic effect" or "biological water", polymer scientists usually prefer universal scaling laws, etc. and forget that the tiny solvent molecules represent an important component of the system.

The second criterion was the choice of fluorescence techniques itself. We wanted to include examples of both relatively widely used techniques like NRET or fluorescence anisotropy and show their specific application, and also give some examples of techniques little used in polymer research, like SRM or FCS. One of goals was the "advertisement" of SRM because, in contrast to FCS that is finding supporters among other POLYAMPHI members [152, 155], SRM is a "Cinderella" in polymer science.

The third criterion of the selection derives directly from the main goals of the paper. We wanted to show how computer modeling could help in the interpretation of fluorescence data on complex systems. As already mentioned, fluorescence is an indirect technique and an unambiguous interpretation needs pieces of independent information. In our studies, we combined fluorescence with a number of experimental techniques and computer simulations. We hope that we have persuaded readers that computer modeling offers a deep insight into the behavior of studied systems and, besides being a semi-quantitative reproduction of observed trends, can yield new hints for experimental research.

Acknowledgments The authors would like to acknowledge the EU support (Marie Curie MRTN-CT-2003-505027, "POLYAMPHI"), the support of the Ministry of Education, Youths and Sports of the Czech Republic (Research Plan MSM0021620857), the Grant Agency of the Czech Republic (203/07/0659), the Grant Agency of the Academy of Sciences of the Czech Republic (IAA400400621, IAA401110702, and KJB401110701) and the Grant Agency of Charles University (43-257269).

References

1. Jablonski A (1935) Z Phys 94:38
2. Levine IN (1975) Molecular spectroscopy. Wiley, London

3. Turro NJ (1991) Modern molecular photochemistry. University Science Books, Sausalito, California
4. Franck J (1926) Trans Faraday Soc 21:536
5. Condon E (1926) Phys Rev 28:1182
6. Fleming GR (1986) Chemical applications of ultrafast spectroscopy. Oxford University Press, New York
7. Beer M, Longuet-Higgins HC (1955) J Chem Phys 23:1390
8. Lakowicz JR (1983) Principles of fluorescence spectroscopy. Plenum, New York
9. Debye P (1945) Polar molecules. Dover, New York
10. Favro LD (1960) Phys Rew 119:53
11. Michl J, Thulstrup EW (1986) Spectroscopy with polarized light. VCH, New York
12. Procházka K, Medhage B, Mukhtar E, Almgren M, Svoboda P, Trnìná J, Bednář B (1993) Polymer 34:103
13. Birks JB (1970) Photophysics of aromatic molecules. Wiley, London
14. Valeur B, Monnerie L (1976) J Polym Sci Pt B-Polym Phys 14:11
15. Stubbs CD, Williams BW (1992) In: Lakowicz JR (ed) Topics in fluorescence spectroscopy: biochemical applications. Plenum, New York, p 231
16. Lentz BR (1993) Chem Phys Lipids 64:99
17. Gidwani A, Holowka D, Baird B (2001) Biochemistry 40:12422
18. Klymchenko AS, Duportail G, Demchenko AP, Mely Y (2004) Biophys J 86:2929
19. Ha TJ, Ting AY, Liang J, Caldwell WB, Deniz AA, Chemla DS, Schultz PG, Weiss S (1999) Proc Natl Acad Sci USA 96:893
20. Swaminathan R, Hoang CP, Verkman AS (1997) Biophys J 72:1900
21. Heikal AA, Hess ST, Baird GS, Tsien RY, Webb WW (2000) Proc Natl Acad Sci USA 97:11996
22. Volkmer A, Subramaniam V, Birch DJS, Jovin TM (2000) Biophys J 78:1589
23. Birch DJS, Geddes CD (2000) Phys Rev E 62:2977
24. Kujawa P, Aseyev V, Tenhu H, Winnik FM (2006) Macromolecules 39:7686
25. Katsumoto Y, Tsunomori F, Ushiki H, Letamendia L, Rouch J (2001) Eur Polym J 37:475
26. Wang B, Liu MZ, Chen Y, Liang R, Chen SL, Jin SP (2007) J Appl Polym Sci 104:1714
27. Pistolis G, Andreopoulou AK, Malliaris A, Kallitsis JK (2005) J Phys Chem B 109:11538
28. Viovy JL, Monnerie L, Merola F (1985) Macromolecules 18:1130
29. Viovy JL, Frank CW, Monnerie L (1985) Macromolecules 18:2606
30. Monnerie L (1991) J Non-Cryst Solids 131:755
31. Adams S, Adolf DB (1999) Macromolecules 32:3136
32. Kiserow D, Procházka K, Ramireddy C, Tuzar Z, Munk P, Webber SE (1992) Macromolecules 25:461
33. Sen S, Sukul D, Dutta P, Bhattacharyya K (2001) J Phys Chem A 105:7495
34. Kim C, Lee SC, Shin JH, Kwon IC, Jeong SY (2000) Macromolecules 33:7448
35. Sýkora J, Slavíček P, Jungwirth P, Barucha J, Hof M (2007) J Phys Chem B 111:5869
36. Chakrabarty A, Chakraborty D, Seth D, Hazra P, Sarkar N (2005) Chem Phys Lett 412:255
37. Sen P, Roy D, Mondal SK, Sahu K, Ghosh S, Bhattacharyya K (2005) J Phys Chem A 109:9716
38. Lang B, Angulo G, Vauthey E (2006) J Phys Chem A 110:7028
39. Hutterer R, Schneider FW, Sprinz H, Hof M (1996) Biophys Chem 61:151
40. Moyano F, Biasutti MA, Silber JJ, Correa NM (2006) J Phys Chem B 110:11838
41. Rowe BA, Neal SL (2006) J Phys Chem B (2006) 110:15021
42. Lippert E (1957) Z Elektrochem 61:962
43. Badea MG, DeToma RP, Brand L (1978) Biophys J 24:197
44. Chattopadhyay A, Mukherjee S (1993) Biochemistry 32:3804
45. Hutterer R, Schneider FW, Lanig H, Hof M (1997) Biochim Biophys Acta – Biomembranes 1323:195
46. Gafni A, DeToma RP, Manrow RE, Brand L (1977) Biophys J 17:155
47. Toptygin D, Gronenborn AM, Brand L (2006) J Phys Chem B 10:26292

48. Brauns, EB, Madaras ML, Coleman, RS, Murphy CJ, Berg MA (1999) J Am Chem Soc 121:11644
49. Middelhoek ER, Vandermeulen P, Verhoeven JW, Glasbeek M (1995) Chem Phys 198:373
50. Gulbinas V, Markovitsi D, Gustavsson T, Karpicz R, Veber M (2000) J Phys Chem A 104:5181
51. Chakrabarty D, Charkraborty A, Seth D, Sarkar N (2005) J Phys Chem A 109:1764
52. Cichos F, Willert A, Rempel U, von Borczykowski C (1997) J Phys Chem A 101:8179
53. Molotsky T, Huppert D (2003) J Phys Chem A 107:8449
54. Mukherjee S, Sahu K, Roy D, Mondal SK, Bhattacharyya K (2004) Chem Phys Lett 384:128
55. Sen P, Ghosh S, Sahu K, Mondal SK, Roy D, Bhattacharyya K (2006) J Chem Phys 124:204905
56. Adikhari A, Dey S, Das DK, Mandal U, Ghosh S, Bhattacharyya K (2008) J Phys Chem B 112:6350
57. Kasha M (1952) J Chem Phys 20:71
58. Stern O, Volmer M (1919) Phys Z 20:183
59. Förster T (1949) Z Naturforsch 4A:321
60. Förster T (1959) Discuss Faraday Soc 7:27
61. Van Der Meer WB, Coker G, Chen SS-Y (1991) Resonance energy transfer. Wiley, New York
62. Dale RE, Eisinger J, Blumberg WE (1979) Biophys J 26:161
63. Eisinger J, Blumberg WE, Dale RE (1981) Biophys J 33:155
64. Chee CK, Rimmer S, Soutar I, Swanson L (2001) Polymer 42:5079
65. Kuzmenkina EV, Heyes CD, Nienhaus GU (2005) Proc Natl Acad Sci USA 102:15471
66. Suwa M, Hashidzume A, Morishima Y, Nakato T, Tomida M (2000) Macromolecules 33:7884
67. Holappa S, Kantonen L, Winnik FM, Tenhu H (2004) Macromolecules 37:7008
68. Dias FB, Knaapila M, Monkman AP, Burrows HD (2006) Macromolecules 39:1598
69. Pham HH, Farinha JPS, Winnik MA (2000) Macromolecules 33:5850
70. Xiang ML, Jiang M, Zhang YB, Wu C, Feng LX (1997) Macromolecules 30:2313
71. Feng JR, Yekta A, Winnik MA (1996) Chem Phys Lett 260:296
72. Torchilin VP, Levchenko TS, Whiteman KR, Yaroslavov AA, Tsatsakis AM, Rizos AK, Michailova EV, Shtilman MI (2001) Biomaterials 22:3035
73. Mizusaki M, Morishima Y, Winnik FM (1999) Macromolecules 32:4317
74. Barros TC, Adronov A, Winnik FM, Bohne C (1997) Langmuir 13:6089
75. Magde D, Elson EL, Webb WW (1974) Biopolymers 13:29
76. Schwille P, Bieschke J, Oehlenschlager F (1997) Biophys Chem 66:211
77. Schwille P (2001) Cell Biochem Biophys 34:383
78. Sanchez SA, Gratton E (2005) Acc Chem Res 38:469
79. Remaut K, Lucas B, Raemdonck K, Beckmans K, Demeester J, De Smedt SC (2007) J Controlled Release 121:49
80. Humpolíčková J, Beranová L, Štěpánek M, Benda A, Procházka K, Hof M (2008) J Phys Chem B 112:16823
81. Zettl H, Hafner W, Boker A, Schmalz H, Lanzendorfer M, Müller AHE, Krausch G (2004) Macromolecules 37:1917
82. Bonne TB, Papadakis CM, Ludtke K, Jordan R (2006) Colloid Polym Sci 285:491
83. Pecora BJ, Pecora R (2000) Dynamic light scattering. Wiley, New York
84. Humpolíčková J, Procházka K, Hof M, Tuzar Z, Špírková M (2003) Langmuir 19:4119
85. Wu B, Chen Y, Muller JD (2008) Biophys J 94:2800
86. Bednář B, Trnˇiná J, Svoboda P, Vajda S, Fidler V, Procházka K (1991) Macromolecules 24:2054
87. Košovan P, Limpouchová Z, Procházka K (2006) Macromolecules 39:3458
88. Štěpánek M, Matějíček P, Humpolíčková J, Procházka K (2005) Langmuir 21:10783
89. Humpolíčková J, Štěpánek M, Procházka K, Hof M (2005) J Phys Chem A 109:10803
90. Matějíček P, Podhájecká K, Humpolíčková J, Uhlík F, Jelínek K, Limpouchová Z, Procházka K, Špírková M (2004) Macromolecules 37:10141
91. Uhlík F, Limpouchová Z., Jelínek K, Procházka K (2004) J Phys Chem 121:2367

92. Uhlík F, Limpouchová Z, Matějíček P, Procházka K, Tuzar Z, Webber SE (2002) Macromolecules 35:9497
93. Matějíček P, Uhlík F, Limpouchová Z, Procházka K, Tuzar Z, Webber SE (2002) Macromolecules 35:9487
94. Matějíček P, Humpolíčková J, Procházka K, Tuzar Z, Špírková M, Hof M, Webber SE (2003) J Phys Chem B 107:8232
95. Uhlík F, Limpouchová Z, Jelínek K, Procházka K (2003) J Phys Chem 118:11258
96. Matějíček P, Uhlík F, Limpouchová Z, Procházka K, Tuzar Z, Webber SE (2002) Collect Czech Chem Commun 67:531
97. Štěpánek M, Humpolíčková J, Procházka K, Hof M, Tuzar Z, Špírková M, Wolff T (2003) Collect Czech Chem Commun 68:2120
98. Štěpánek M, Matějíček P, Humpolíčková J, Havránková J, Podhajecká K, Špírková M, Tuzar Z, Tsitsilianis C, Procházka K (2005) Polymer 46:10493
99. Dobrynin AV, Rubinstein M, Obukhov SP (1996) Macromolecules 29:2974
100. Dautzenberg H, Jaeger W, Kotz BPJ, Seidel C, Stscherbina D (1994) Polyelectrolytes: formation, characterization and applications. Hanser, Munich
101. Khokhlov AR (1980) J Phys Chem A 13:979
102. Kantor Y, Kardar M (1995) Phys Rev E 51:1299
103. Lord Rayleigh (1882) Philos Mag 14:184
104. Limbach HJ, Holm C (2003) J Phys Chem. B 32:8041
105. Limbach HJ, Holm C, Kremer K (2004) Macromol Symp 211:43
106. Raphael E, Joanny JF (1990) Europhys Lett 13:623
107. Uyaver S, Seidel C (2003) Europhys Lett 64:536
108. Uyaver S, Seidel C (2004) J Phys Chem B 180:18804
109. Ulrich S, Laguecir A, Stoll S (2005) J Chem Phys 122:094911
110. Laguecir A, Ulrich S, Labille J, Fatin-Rouge N, Stoll S, Buffle J (2006) Eur Polym J 42:1135
111. Borukhov I, Andelman D, Borrega R, Cloitre M, Leibler L, Orland H (2000) J Phys Chem B 104:11027
112. Katchalski A (1951) J Polym Sci 7:393
113. Strauss UP, Schlesinger MS (1978) J Phys Chem 82:571
114. Strauss UP, Schlesinger MS (1978) J Phys Chem 82:1627
115. Strauss UP, Vesnaver G (1975) J Phys Chem 79:1558
116. Strauss UP, Vesnaver G (1975) J Phys Chem 79:2426
117. Wang Y, Morawetz H (1986) Macromolecules 19:1925
118. Ghiggino KP, Tan KL (1985) In: Phillips D (ed) Polymer photophysics. Chapman and Hall, London
119. Popelka S, Machová LK, Rypáček F, Špírková M, Štěpánek M, Matějíček P, Procházka K (2005) Collect Czech Chem Commun 70:1811
120. Matějíček P, Štěpánek M, Uchman M, Procházka K, Špírková M (2006) Collect Czech Chem Commun 71:723
121. Šachl R, Uchman M, Matějíček P, Procházka K, Štěpánek M, Špírková M (2007) Langmuir 23:3395
122. Harada A, Kataoka K (2006) Prog Polym Sci 31:949
123. Polik WF, Burchard W (1983) Macromolecules 16:978
124. Zhou P, Brown W (1990) Macromolecules 23:1131
125. Kinugasa S, Nakahara H, Fudagawa N, Koga Y (1994) Macromolecules 27:6889
126. Polverari M, van de Ven TGM (1996) J Phys Chem 100:13687
127. Duval M. (2000) Macromolecules 33:7862
128. Hammouda B, Ho DL, Kline S (2004) Macromolecules 37:6932
129. De Gennes, PG (1991) C R Acad Sci, Ser II 313:1117
130. Horng ML, Gardecki JA, Papazyan A, Maroncelli M (1995) J Phys Chem 99:17311
131. Fee RS, Maroncelli M (1994) Chem Phys 183:235
132. Martin TJ, Procházka K, Munk P, Webber SE (1996) Macromolecules 29:6071
133. Bieze TWN, Barnes AC, Huige CJM, Enderby JE, Leyte JC (1994) J Phys Chem 98:6568
134. Blandamer MJ, Fox MF, Powell E, Stafford JW (1967) Makromol Chem 124:222

135. Šachl R, Štěpánek M, Procházka K, Humpolíčková J, Hof M (2008) Langmuir 24:288
136. Bonacucina G, Cespi M, Misici-Falzi M, Palmieri GF (2009) J Pharm Sci 98:1
137. Zhao Q, Ni PH (2006) Prog Chem 18:768
138. Yasugi K, Nakamura T, Nagasaki Y, Kato M, Kataoka K (1999) Macromolecules 32:8024
139. Otsuka H, Nagasaki Y, Kataoka K (2001) Curr Opin Colloid Interface Sci 6:3
140. Dufresne MH, Gauthier MA, Leroux JC (2005) Bioconjugate Chem 16:1027
141. Rieger J, Stoffelbach F, Cui D, Imberty A, Lameignere E, Putaux JL, Jerôme R, Auzely-Velty R (2007) Biomacromolecules 8:2717
142. Hu ZY, Luo F, Pan YF, Hou C, Ren LF, Chen JJ, Wang JW, Zhang YD (2008) J Biomed Mater Res A 85A:797
143. Martin TJ, Webber SE (1995) Macromolecules 28:8845
144. Berlman IB (1973) Energy transfer parameters of aromatic compounds. Academic, New York
145. Shusharina NP, Linse P (2001) Eur Phys J 4:399
146. Micka U, Holm C, Kremer K (1999) Langmuir 15:4033
147. Heitz C, Rawiso M, Francois J (1999) 40:1637
148. Košovan P, Limpouchová Z, Procházka K (2008) Collect Czech Chem Commun 73:439
149. Allen DJ, Tildesley MP (1987) Computer simulation of liquids. Clarendon, Oxford
150. Limbach HJ, Holm C (2001) J Chem Phys 114:9674
151. Morcellet M, Wozniak M (1991) Macromolecules 24:745
152. Porasso RD, Benegas JC, van den Hoop MAGT (1999) J Phys Chem B 103:2361
153. Lide DR, Frederikse HPR (1995) Handbook of chemistry and physics, 76th edn. CRC, Boca Raton, FL
154. Zettl H, Häfner W, Böker A, Schmalz H, Lanzendörfer M, Müller AHE, Krausch G (2004) Macromolecules 37:1917
155. Zettl H, Zettl U, Krausch G, Enderlein J, Ballauff M (2007) Phys Rev E 75:061804